ANGULAR CORRELATION EXPERIMENTS WITH THE $F^{19}(p, \alpha\gamma)O^{16}$ REACTION

Thesis by

Hugh Jack Martin, Jr.

In Partial Fulfillment of the Requirements

for the Degree of

Doctor of Philosophy

California Institute of Technology

Pasadena, California

1956

ACKNOWLEDGMENTS

The author wishes to express his gratitude to Professors T. Lauritsen, C. C. Lauritsen, C. A. Barnes, W. A. Fowler, and R. F. Christy for their assistance and guidance throughout the course of this work. Thanks are also extended to Mr. C. Cook for his assistance during much of the experimental work. The author also wishes to express his appreciation to the General Electric Company for a fellowship during the academic year, 1954-55.

ABSTRACT

A strong-focussing magnetic particle spectrometer was constructed and its properties and performance are discussed. Angular correlation patterns for the $F^{19}(p, \alpha\gamma)O^{16}$ reaction were measured at incident proton energies of 874, 935, 1250, 1280, 1346, and 1372 kev. Confirmation of previous level assignments was found in all cases. Some level parameters, connected with alpha emission, are evaluated for several resonances and are shown to be consistent with different experimental measurements.

TABLE OF CONTENTS

I. INTRODUCTION

In recent years, the study of the angular distributions of radiation products in nuclear reactions has played an important role in the determination of the geometrical properties of nuclear states. A natural extension of this work for a three-stage process involves an angular correlation between a product particle and a subsequent disintegration, usually a gamma-ray. This has met its greatest success in the reaction $F^{19}(p, \alpha\gamma)O^{16}$, where the angular momentum assignments of the first three gamma-emitting states of the O^{16} nucleus were established by experiments of this type.[1, 2]

The general angular correlation experiment involves an incoming particle beam to initiate the reaction and two detectors which respond to the types of radiation of interest. A coincidence circuit is used to require simultaneous events in the two detectors.

The detectors may be characterized by 1) counting efficiency for particular types of radiation, 2) solid angle, 3) energy or momentum resolution, 4) dead time, and 5) speed of response to an event. A broad classification can be made by considering particle detectors and gamma-ray detectors separately.

Scintillation crystals fulfill the requirements for gamma-ray detection. The pulse size is proportional to the energy of the gamma-ray while response times from 10^{-6} to 10^{-8} seconds are available in the different types of scintillators. Dead times are usually determined by the associated electronic equipment rather than by the crystal. The major disadvantage is the inability of

the crystal to discriminate between different gamma rays. Consequently, non-coincident gamma rays can control the rate at which desired gammas can be accepted, and therefore can control the feasibility of the experiment.

This disadvantage becomes more pronounced when thin scintillation crystals are used as particle detectors. Extraneous particles are generally abundant and absorption or other techniques must be used to remove them. Standard particle spectrometers overcome this disadvantage and may retain most of the advantages of the crystal by using it as a detector after the particle analysis is completed. A minor inconvenience is the time of flight through the spectrometer; a major one is the smaller solid angle usually found in such spectrometers.

The incorporation of a particle spectrometer into angular correlation experiments then proves desirable in giving greater versatility to the experimental arrangement, and increasing its possible future use. The general design concept of particle spectrometers to seek a maximum resolution compromised only by the practical demands of solid angle is modified by the particular problems of this type of experiment. The angular correlation problem emphasizes the solid angle of the instrument and a minimum, rather than a maximum, resolution is of interest.

The two types of magnetic spectrometers considered in this connection are the double-focussing spectrometer and the alternating-gradient spectrometer. The double-focussing spectrometer has been in use for some time,[3, 4] utilizing a small gradient of the magnetic field to focus particles entering it. The alternating-

gradient, or strong-focussing, spectrometer incorporates a principle introduced by Courant, et al.,[5] in 1952, where a large gradient of the magnetic field introduces strong focussing and defocussing properties in two mutually perpendicular planes. Two magnets are combined in such a way as to give an overall focussing effect as is shown in Figure 1.

The alternating-gradient spectrometer, constructed in Kellogg Laboratory and discussed in this report, was employed in investigations of Ne^{20} states formed in the bombardment of F^{19} with protons. In addition to interest in these levels of Ne^{20} for themselves, they appear in several other connections; the recent $F^{19}(p, p'\gamma)F^{19}$ studies[6] of the 109 and 196 Kev low-lying levels in F^{19} and the earlier-mentioned use of the $F^{19}(p, \alpha\gamma)O^{16}$ reaction are examples. An incomplete tabulation of the large number of experiments involving some of the Ne^{20} states is given in Table 1.

TABLE 1

Proton Bombarding Energy	p-p	$F^{19}(p, \alpha)O^{16}$								
		$p-\alpha_1$	$p-\gamma_1$	$\alpha_1-\gamma_1$	$p-\alpha_2$	$\alpha_2-\gamma_2$	$p-\alpha_3$	$\alpha_3-\gamma_3$	$p-\gamma_{2^+3}$	$p(\alpha)-\gamma_3$
874 Kev	x	x	x	x*	x	x	x	x	x	x
935 Kev	x		x	x*	x	x	x	x	x	x
1280 Kev				x	x		x			x
1346 Kev	x			x	x		x			x
1372 Kev	x		x	x	x		x		x	x

The subscripts 1, 2, 3 refer to first three gamma-emitting states in O^{16} in order of ascending γ energy.

*Two experiments performed with γ counter in two different planes.

The alpha-gamma correlation studies which were undertaken involve the $F^{19}(p, \alpha\gamma)O^{16}$ reaction and these results are combined with other closely related experiments to determine some level parameters.

II. THE ALTERNATING-GRADIENT MAGNETIC SPECTROMETER

1. Theory

The double lens magnetic system was discussed briefly by Courant, et al.,[5] in their first paper on the subject of strong focussing and this discussion was amplified in some detail in a later paper by Sternheimer.[7] We follow the approach used by Judd[8] for the double-focussing spectrometer and draw heavily upon the optical analogy used by him. A single magnetic lens will be treated first and the extension to a double lens system will be a natural one.

A cylindrical coordinate system, r, ϕ, z is used with the magnetic field confined between the planes $\phi = 0$ and $\phi = \Phi$, the field having the form

$$\vec{B} = \vec{e}_z B_0 \left[1 - n \frac{r - r_0}{r_0} \right] - \vec{e}_r B_0 n \frac{z}{r_0}$$

If a point source of monoenergetic charged particles having mass m, velocity v, and charge e is placed outside of the field on a line tangent to the circle $r = r_0$, $z = 0$ at the edge of the field, then, setting $B_0 = -\frac{mv}{e r_0}$ allows particles entering the field normally to travel along the circle and emerge normal to the other side of the field. This defines the optic axis of the system.

The linearized equations of motion are presented in Appendix I and have the solutions

$$z = C \sin \sqrt{n}(\phi - c) \qquad \rho = r - 1 = B \sin \sqrt{1-n}\,\Phi$$

where C, c, B, and b are constants. All lengths are measured in units of r_0.

If n is taken to be large compared to one, then the solution for ρ can be derived from the solution for z by making the substitution $i\sqrt{n} = \sqrt{n}$. The z solution is considered first. For a single lens, the focal length is

$$f_1 = \frac{1}{\sqrt{n}\,\sin\sqrt{n}\,\Phi}$$

As illustrated in Figure 2, the principal plane lies inside the field edges a distance

$$P_1 = \frac{1 - \cos\sqrt{n}\,\Phi}{\sqrt{n}\,\sin\sqrt{n}\,\Phi}$$

Substitution of $i\sqrt{n}$ for $\sqrt{n}$ gives a divergent lens with

$$f_2 = -\frac{1}{\sqrt{n}\,\sinh\sqrt{n}\,\Phi} \qquad P_2 = \frac{\cosh\sqrt{n}\,\Phi - 1}{\sqrt{n}\,\sinh\sqrt{n}\,\Phi}$$

A two lens system is now considered in which the lenses are either convergent, then divergent, or the converse depending upon the coordinate of interest. The alternation is achieved by simply changing the sign of n for the second lens. For simplicity, the magnet lengths will be taken equal to Φ and the absolute value of n will be the same in each magnet. Then the reciprocal focal length for both the convergent-divergent case and divergent-convergent case may be written

$$\frac{1}{f} = \frac{1}{f_1} + \frac{1}{f_2} - \frac{\Delta}{f_1 f_2}$$

$$= \cosh\sqrt{n}\,\Phi\,\cos\sqrt{n}\,\Phi\left[\tan\sqrt{n}\,\Phi - \tanh\sqrt{n}\,\Phi + d\sqrt{n}\,\tan\sqrt{n}\,\Phi\tanh\sqrt{n}\,\Phi\right]$$

where d is introduced as the separation of the two magnets. The

separation of the unit planes of the two systems is given by $\Delta = d + p_1 + p_2$. The location of the exit principal plane differs for the two cases and is for the convergent-divergent case

$$P = p_2 + \frac{\Delta f}{f_1}$$

$$= f\left\{1 + \cosh\sqrt{n}\Phi\cos\sqrt{n}\Phi\left[\tan\sqrt{n}\Phi\tanh\sqrt{n}\Phi - 1 + d\sqrt{n}\tan\sqrt{n}\Phi\right]\right\}$$

The divergent-convergent case is

$$P' = p_1 + \frac{\Delta f}{f_2}$$

$$= f\left\{1 - \cosh\sqrt{n}\Phi\cos\sqrt{n}\Phi\left[\tan\sqrt{n}\Phi\tanh\sqrt{n}\Phi + 1 + d\sqrt{n}\tanh\sqrt{n}\Phi\right]\right\}$$

Now the relations which are of interest may be considered. The first of these is the property of double-focussing which requires that the image positions for the two cases be located at the same physical position for a common source. This can be satisfied in two ways as is easily seen in Figure 3. Either the principal planes must be symmetrically located, i.e. $p = p'$, or the source and image positions must lie equidistant from the field edges. The first condition imposes the relation

$$d\sqrt{n} = \frac{-2\tanh\sqrt{n}\Phi\tan\sqrt{n}\Phi}{\tan\sqrt{n}\Phi + \tanh\sqrt{n}\Phi}$$

but is not practical because the detector or source must be located within the field region in order to satisfy it. The second condition requires

$$d\sqrt{n} = \frac{(\tanh\sqrt{n}\Phi - \tan\sqrt{n}\Phi)^2 n d_o^2 + 2 d_o\sqrt{n} + \tan\sqrt{n}\Phi + \tanh\sqrt{n}\Phi}{d_o^2 n \tan\sqrt{n}\Phi \tanh\sqrt{n}\Phi + d_o\sqrt{n}(\tan\sqrt{n}\Phi - \tanh\sqrt{n}\Phi) - 1}$$

where d_o is the distance from the source to the field edge as shown in Figure 1. This condition is related to the optical theorem stating that any system with the source and image distance greater than four times the focal length apart has two possible locations of the principal planes.

The magnification can be found easily by the optical analogy and is chosen to be positive when it gives an inverted image. For the convergent-divergent case, we have

$$M_{CD} = \frac{d_o + P}{f} - 1$$

$$= \sinh\sqrt{n}\Phi \sin\sqrt{n}\Phi - \cosh\sqrt{n}\Phi \cos\sqrt{n}\Phi + d\sqrt{n} \sin\sqrt{n}\Phi \cosh\sqrt{n}\Phi$$

$$+ d_o\sqrt{n}\left[\sin\sqrt{n}\Phi \cosh\sqrt{n}\Phi - \sinh\sqrt{n}\Phi \cos\sqrt{n}\Phi + d\sqrt{n} \sin\sqrt{n}\Phi \sinh\sqrt{n}\Phi\right]$$

and the magnification for the divergent-convergent case is simply the reciprocal of this. The dispersion and resolution follow from the formulae given by Judd[8] and can be written

$$D = \frac{\delta\rho}{\frac{\delta p}{p}} = \frac{1 + M_r}{n} \qquad R = \frac{P}{\delta p} = \frac{1 + 1/M_r}{n \alpha s}$$

The M_r represents the magnification in the z = 0 plane which is chosen to be the divergent-convergent case for reasons which will become clear. The spectrometer then has an orientation similar to that shown in Figure 1. s is the source width and a is a number larger than unity depending on the aberrations.

The solid angle is the one remaining quantity of interest.

The maximum cross-sectional dimensions of the spectrometer are taken to be independent of Φ and are written A r_o^2. Because the beam attains its maximum deviation in the convergent magnet for both cases, the effective area has the shape of an ellipse and we write

$$\Omega = \pi (\tan \alpha_{max})_{CD} (\tan \alpha_{max})_{DC}$$

where the tangents of the maximum angles of acceptance for the divergent-convergent and the convergent-divergent cases are indicated. If the maximum deviation is the same for the two cases and is designated by y_{max}, then

$$\frac{\Omega}{A} = M_{DC} \frac{(\tan \alpha_{max})^2_{CD}}{y^2_{max}}$$

$$= \frac{n}{1 + n d_o^2} M_{DC}$$

This completes the first-order theory. The more practical consequences of fringing fields and second-order theory will be discussed for the particular spectrometer that was constructed.

2. Design Criteria

The number $\sqrt{n}$ can be considered a wave number and an increase in $\sqrt{n}$ then implies a shorter wavelength, moving the image towards the source. An obvious comparison is made; the alternating-gradient spectrometer can focus particles with less iron and in a shorter distance than the double-focussing spectrometer. The effect on the other properties of the spectrometer is more subtle and is discussed in more detail.

The double-focussing spectrometer is thoroughly discussed by Judd[8] and his results are easily summarized. A value of n equal to 0.5 insures double-focussing and maximizes the solid angle. Choice of the source distance, d_o, fixes the solid angle and leaves one remaining parameter, the magnet length, Φ, to determine the resolution. Decreasing Φ is expected to decrease the resolution. A more important change is the rapid increase in the total distance between source and image as Φ decreases. This is shown in Figure 4 and the resolution is also shown there as a much less sensitive function of Φ. This is to be expected because an increase in the overall length tends to compensate for the smaller region of magnetic field.

The analysis of an alternating-gradient spectrometer is not so direct. The parameters n, Φ, and d_o all affect the solid angle and the resolution in a rather intricate fashion. To simplify the discussion, a severe restriction will be placed upon the defining aperture of the magnets. The magnetic field in the $z = 0$ plane will increase from a value of zero to twice the value of the equilibrium orbit field across the diameter of the aperture. The aperture is chosen to be circular. This arrangement agrees with the strong-focussing spectrometer that was constructed, but has two major disadvantages which will be discussed.

The first effect of the restriction appears in the value of the magnetic field on the equilibrium orbit. This value will be one-third to one-half of the value of the flux density in the iron. A double-focussing spectrometer, on the other hand, has an equilibrium orbit field comparable to the flux density in the iron. If equal

magnetic rigidities are required in the two types of spectrometers, the radius of curvature of the alternating-gradient spectrometer must be about twice that of the double-focussing spectrometer.

A more serious limitation has been placed on the area of the aperture. This area is $A = \pi y_{max}^2$ (remembering that y_{max} is expressed in units of r_o) and the shape of the field invokes the relation, $n = 1/y_{max}$. The area is then a very strong function of n and the discussion must be limited to moderate values of n.

Figures 5 through 7 depict the various characteristics of the strong-focussing spectrometer. The solid angle and resolution show the same kind of dependence on $\sqrt{n}\,\Phi$ in Figure 6 because of a rapid change in magnification as the magnet length is changed. Variation of the solid angle with n follows a curve similar to the resolution curve in Figure 7. Removal of the aperture restriction improves the solid angle situation considerably and makes higher values of n desirable. Larger values of n may also be used when a large radius of curvature, r_o, is used. All lengths have been expressed in units of r_o, but might have been equally well expressed in units of $r_o/\sqrt{n}$. Resolution and solid angle values depend on r_o through the source size and area of the aperture and this dependence must be recognized in comparisons between the two types of spectrometers.

The spectrometer properties shown in Figures 5 to 7 describe a low-resolution instrument. Larger solid angles appear to be more easily achieved than in the double-focussing spectrometer, although this difference between the two spectrometers is not very striking. In general, the alternating-gradient spectrometer appears to offer better particle collection properties than the double-focussing magnet.

The shorter path length of the strong-focussing spectrometer might also be of interest in a study of unstable particles.

High resolution strong-focussing spectrometers involve intermediate focussing effects. These are not discussed because of aberrations which would tend to limit their usefulness.

3. Physical Features

A strong-focussing spectrometer, designed by Dr. A. Kraus, presently of Rice Institute, was constructed. Its design characteristics may be summarized

Max Energy Proton Accepted	8 Mev
Max Equilibrium Orbit Field	5000 gauss
Radius of Curvature	80 cm
n	25
Φ	$14^{o}55'$
d_o	16 cm
d	12 cm
L	85.6 cm
y_{max}	1.25 in.
Ω	.012 steradians
R (for .125" source)	63

The yoke of the magnet is made of a 0.18% carbon steel which has a linear relation between B and H for fields up to 15,000 gauss. The original pole pieces were made from boilerplate of a somewhat higher carbon content and were later replaced by pole pieces made of Armco iron. A cross-section of the entry magnet with some of its physical dimensions is shown in Figure 8. The pole pieces are rectangular hyperbolas with a reflector pole replacing the other two poles necessary to give the field the desired

shape. A vacuum chamber of non-magnetic stainless steel was pressed between the two magnet halves in order to fit the contour of the pole pieces.

The coils are 35 turns of .051" x .153" enameled magnet wire and there are sixteen coils for each magnet. Each coil is wrapped with fiberglas tape and lies between two copper cooling plates .065" thick with 3/16" copper tubing soldered to their outside edge. After the coils were placed in the magnet they were impregnated under vacuum with a thermosetting plastic cement. In three of the magnet halves, the resistance between the coils and the magnet exceeded 20 megohms. The fourth section of the magnets has a resistance of only 100,000 ohms to ground because of leakage around the external leads to the coils.

Power is supplied by a 35-kilowatt generator and the magnets are operated in parallel. Each magnet has a resistance of 1.6 ohms and approximately 34,000 ampere-turns are available at the maximum output of the generator.

The magnetic field is measured by a fluxmeter located in the field just outside the pole pieces at a position designated by A in Figure 8. Two coils, each one-half inch in diameter and wound with 90 turns of #36 formvar enameled wire, are suspended from a quartz fiber. Oppositely directed currents in the two coils give the effect of two oppositely directed magnetic dipoles and the resulting couple on the quartz fiber depends on the magnetic field gradient rather than the actual field. This design was suggested by Dr. C. C. Lauritsen as a method of achieving vertical suspension of the coils.

4. Field Measurements

Measurements were made of the magnetic field to study its gradient, the effective fringing field, and saturation difficulties. The field inside the magnet was measured at a number of different depths. The experimental points are shown in Figure 9, and a value n = 25.5 is found. The field varies linearly except near its edges.

The fringing field along the equilibrium orbit was measured and relative values are shown in part (b) of Figure 10. The slow drop to zero field is partly a result of the projection of the coils 6 centimeters beyond the magnet ends. Part (a) of Figure 10 shows the effective n in the fringing field. It does not show the variation in the size of the region over which this gradient existed.

An empirical rule for the effect of the fringing field on the magnet length is given by Sternheimer[7] and is

$$\ell_{eff} = \ell_0 + \left[2\,(0.5 \text{ to } 0.75) \quad \text{times gap width}\right]$$

This gives the effective length as a function of the gap width so that the effective magnet face does not parallel the true magnet face. The gap width on the equilibrium orbit indicates an effective magnet sector of 17.8° in agreement with estimates made from both parts of Figure 10.

The effective length of a single magnet was also studied by passing a proton beam through it, the beam being first deflected by an a-c magnet simulating a source. The source-image positions found in this way could be related to the effective magnet

length and indicated a correction only 30-50% that given by the field measurements. Final source and image positions of the double lens system agree with the lesser effect.

Fringing field problems are of interest in a magnet of this type because they provide an important correction to the theoretical design. For example, in this particular magnet fringing field effects might have been expected to increase the magnet lengths by 20%, a circumstance which would have made it difficult to arrange easy access to the source and image positions with the planned physical arrangement. Fortunately, the fringing fields played a much less important role.

Saturation effects in the magnetic field were an unanticipated limiting factor in the maximum energy particle which could be analyzed. Calculations of the flux density in the pole pieces compared to the field along the equilibrium orbit indicated a flux density of about $2.7B_o$. This would imply that the magnet should achieve its design values.

Differential saturation was first suspected because of the large variation in gap width, but was disproved by measurements at different positions on the gap. These measurements are shown in Figure 11. Measurements were then made of the amount of flux carried in each leg of the magnet. These measurements are shown in Figure 12. A slight indication of more rapid saturation in the leg attached to the reflector pole is found and can be explained by leakage flux. Both legs display saturation effects, however.

Two possible sources of saturation remain. At sharp turns in the flux path in the iron, a smaller effective area would limit the

total flux. This would require that the effective area be only 65% of the actual area and is not very probable. The second possible explanation is the steel. Saturation begins at a flux density somewhat higher than 9200 gauss. The specifications on the steel state that a flux density of nearly 15,000 gauss is obtainable before saturation effects start. This does not seem consistent with the high carbon content of the material and a comparison with boilerplate of about the same carbon content implies saturation would begin at flux densities between 9,000 to 10,000 gauss.

The uniformity of the saturation effects shown in Figure 11 implies that the focussing properties of the spectrometer should not be damaged by it. Limitation of the energy of protons that can be accepted by the spectrometer is caused by saturation effects and the maximum output of the generator gives a field capable of analyzing 5.9 Mev protons.

5. Focussing Problems

The spectrometer was adjusted by using the proton beam from the 2 Mev electrostatic generator in Kellogg Laboratory. This passed between the poles of a small d-c magnet which could deflect it through angles of 5 or 6 degrees simulating a source. By rotating the d-c magnet around the beam individual rays passing through the spectrometer could be studied and focussing conditions analyzed in detail. Vertical focussing requirements were the important factor in determining the source position while horizontal focussing requirements controlled the image position. The reasons for this will emerge in the following discussion.

Of more immediate interest were aberrations appearing in the horizontal focussing. The two extreme rays were found to intersect inside of the central ray. This effect is predicted by the second-order theory given in Appendix I, but the theory gave a result nearly twice the observed result. The condition was partially corrected by adding extra length to the pole pieces in such a way as to bend the inside ray and the central ray more, in order to intersect the outside ray at the same point. This extra length as a function of ρ is given in Appendix I.

A smeared source, such as might be encountered by using a gas target, is considered next. Motion of a point source along two mutually perpendicular lines will be considered descriptive of the depth of focus of the instrument. Movement of the source along a line in the $z = 0$ plane perpendicular to the equilibrium orbit is not considered because the exit slit of the spectrometer is taken as equal to the magnification of the source in this direction. Any source motion along this axis would then move the image out of the slit.

Movement of the source along the equilibrium orbit is considered first. Figure 3 allows some immediate comment about the convergent-divergent case corresponding to the vertical plane. The source lies very close to the focal plane so a small motion forward will give a large defocussing effect; similarly, a small motion backward brings the image point into the field rapidly and gives a defocussing effect. A depth of about one centimeter, indicated by both theory and experiment, gives a 50% or less loss in intensity. The reverse of the above argument applies to the

horizontal focussing which is only slightly affected by the source.

A more noticeable effect occurs for motion of the source along a vertical axis perpendicular to the equilibrium orbit. Any motion along this axis is greatly magnified in the exit beam and the size of the detector is expected to become a critical factor. Experimentally it was found that other limitations apparently make this motion twice as critical as would be expected from the magnification. No explanation of this behavior has appeared.

III. THE EXPERIMENTAL ARRANGEMENT AND EXPERIMENTAL CORRECTIONS

1. Experimental Apparatus

The protons initiating the reactions were accelerated in a 2 Mev electrostatic generator and were analyzed in energy by a 90^{o} double focussing magnet. The beam passed through the magnetic analyzer and then passed between two adjustable horizontal slits that determined the energy resolution of the beam. The slit separation varied between 1/32" and 1/16" depending on the required beam intensity and the energy resolution was between 0.1% and 0.2%. A rotating vertical slit shown in Figure 14 determined the width of the beam. In general, the cross-sectional area of the incoming beam was about 1 mm^2.

Top and side views of the target chamber are shown in Figures 13 and 14. The target chamber was made of Lucite and had an outside diameter of $2\frac{1}{2}$" and a 1/8" wall. The targets were made by evaporating CaF_2 on 5 to 10 mil thick copper foil. The foil was clamped in an aluminum target holder constructed so that the face of the foil was on the axis of the target chamber when the target holder was in place. A stainless steel tube holding the target holder could be rotated and the face of the target was set at an angle of 45^{o} to the incoming beam during the experiments.

A quartz disk was lowered into the path of the beam for alignment purposes. The shadow of the target in the beam was used to adjust the beam to pass through the axis of the target chamber, the direction of the beam being altered by rotating the analyzing magnet slightly. The axis of the rotating vertical slit was

then adjusted to pass through the beam and this gave a measure of the beam direction.

The gamma detector is shown in Figure 15. The front face of the $1\frac{1}{2}$"x$1\frac{1}{2}$" cylindrical NaI crystal was located 2-1/4" from the axis of the target chamber. The container for the crystal was sealed to a Dumont 6292 photomultiplier tube and the container and the tube were encased in the various magnetic shields depicted in Figure 15. The complete counter was mounted on an aluminum plate and could be rotated about the axis of the target chamber. The plate was supported at the front by a bearing below the target chamber and the rear of the plate was supported by a rod fastened to a bearing near the ceiling.

The outermost casing of the gamma counter was removed and used in the angular calibration of the gamma detector. The casing was placed in position on the aluminum plate and a plug with a peephole in its center was placed in the rear end of the casing. The peephole, the beam, and the vertical defining slits were then brought into line to give the zero angle reading of the detector. This was reproducible to $1/4^{\circ}$. Plugs with peepholes were next placed in both ends of the casing and the peepholes were aligned with the beam. This provided a check on the earlier alignment and placed the axis of the counter in the same horizontal plane as the beam.

Angular calibration of the magnetic spectrometer was carried out by using elastically scattered protons. A vertical slit, .005" wide, was rotated on a circle $1\frac{1}{2}$" in diameter about the axis of the target chamber, while bombarding a copper target with protons. The slit was first rotated across the incoming proton beam to provide a zero and was then rotated across the aperture of the magnet.

The number of protons passing through the spectrometer was recorded as a function of the angular position of the slit and determined the angle of the spectrometer to an accuracy of $1/4^{o}$ to $1/2^{o}$. Similar measurements were made with a horizontal slit in order to ascertain that the incoming proton beam and the alpha detector were in the same horizontal plane. Some of the vertical and horizontal measurements are shown in Figure 16.

The alpha detector was placed 1-1/4" beyond the exit slit of the magnetic spectrometer. A CsI crystal, 1/2"x5/8" and .005" thick, was cemented to a 1.16" thick glass plate and the glass plate was sealed to a Dumont 6291 photomultiplier tube. The crystal and the face of the tube were in the vacuum. Magnetic shields around the tube protected the counter from the fringing field of the spectrometer.

A block diagram of the electronic equipment is shown in Figure 17. The gamma channel was monitored by two discriminators. One discriminator accepted only the pair peak of the gamma spectrum while the other discriminator accepted most of the spectrum. The ratio of counts from the two discriminators then provided a check on the gamma counter gain.

The coincidence mixer had a resolving time of 0.35 microseconds which was slightly shorter than the rise time of the input pulses in the alpha and gamma channels. This resolving time was determined by uniform pulses taken from blocking oscillators which were triggered by the input pulses. Variations in the triggering time were caused by variations in pulse size in the gamma channel and this resulted in a loss of true coincidences. This loss was minimized by placing a 0.1 microsecond delay line in the alpha

channel. The size of this delay was determined by putting common pulses into the two channels and then adjusting their sizes to agree with experimental conditions. Delays were then placed in the individual channels until the number of coincidences was maximized.

A 2.1 microsecond delay line was placed in the alpha channel when only random coincidences were to be counted.

2. Experimental Corrections

Modifications of the experimental angular correlation pattern were necessary for comparison with theoretical predictions. Experimental corrections resulted from 1) the accidental coincidence counting rate, 2) geometrical, absorption, and magnetic effects on the gamma counter efficiency, and 3) the angular resolution of the radiation detectors. These corrections will be discussed in more detail.

Accidental Coincidence Counting Rate. The number of accidental coincidence counts occurring during a run can be written[9]

$$N_a = K \frac{2\tau}{t} N_\alpha N_\gamma \qquad k = \frac{\langle n^2(t) \rangle_{av}}{\langle n(t) \rangle_{av}^2}$$

with

N_a = counts in alpha channel during a run

N = counts in gamma channel during a run

N_a = accidental coincidence counts

τ = resolving time of the coincidence mixer

t = length of run

$n(t)$ = instantaneous disintegration rate

The number K is expected to be unity if the incoming proton beam is constant. In the random coincidence measurements K was found

to vary from 1 to 2.5 and to be more constant in value with smaller beam current. Fluctuations in the value of K were generally large enough to make the experimental measurement of the accidential coincidence rate an integral part of the experiment.

The magnitude of the incoming proton beam determined the total number of disintegrations per second and, therefore, the ratio of true coincidences to random coincidences. The ratio can be written

$$\frac{N_c}{N_a} = \frac{W(\theta)}{2\tau \langle n(t) \rangle_{av} k}$$

N_c = true coincidence counts

The frequency of the accidental coincidence measurements during an experiment was determined by this ratio. In general, 15% to 30% of all of the runs were accidental coincidence measurements.

Geometrical, Absorption, and Magnetic Effects. If the axis of rotation of the gamma counter did not agree with the axis of the target chamber, then the distance from the target to the counter varied as the counter was rotated. A similar effect occurred if the two axes coincided, but the face of the target was not on this axis. Variations of .010" in the distance between the target and the gamma counter resulted in a 1% change in the solid angle of the gamma counter.

Absorption corrections resulted from the passage of gamma rays through the copper target backing or through the aluminum

target holder. Variations in the wall thickness of the target chamber were unimportant.

The different positions of the gamma counter in the fringing field of the magnetic spectrometer led to a variation of the gain of the photomultiplier tube with the angular position of the counter. The total variation of gain due to the magnetic field was measured and found to be less than 1%.

The total effect of these corrections was determined by examining gamma rays from the 935 kev resonance in the $F^{19}(p,\alpha\gamma)O^{16}$ reaction. The angular distribution of these gamma rays had been measured and found to be isotropic to 0.3%.[10] This distribution was measured several times during the experiments and the deviations from isotropy were ascribed to the effects discussed above. The maximum deviation from isotropy was about 2.5% and the indicated corrections were made to the experimental data.

Angular Resolution of the Counters. The angles subtended by the radiation detectors were not negligible and provided an important correction to the experimental angular correlation patterns. In practice it was simpler to modify the theoretical patterns and to use these modified patterns for comparison with the experimental pattern.

The effect of counter resolution on the theoretical angular correlation patterns is extensively discussed in the literature.[11,12] The patterns in the literature are generally expressed as a series of Legendre polynomials. Extension to correlation patterns expressed in powers of the cosine of the angle is given in Appendix II.

The aperture of the magnetic spectrometer was an ellipse

with an eccentricity approaching unity. This aperture was approximated by a straight line of weighted density in the calculations. The gamma detector was a right circular cylinder with its base oriented towards the source. The cylinder was considered uniformly sensitive out to a definite radius and insensitive beyond this radius. The radius was chosen to bring the effective solid angle into agreement with the actual solid angle. This choice gave a radius such that the gamma detector appeared to subtend an angle slightly greater than 30^{o} at the source.

The angles θ, ϕ defined the position of the gamma detector relative to the alpha detector and the theoretical angular correlation patterns were written in the form

$$W(\theta, \phi) = \sum_{m} \sum_{n} a_{nm} \cos^{n}\theta \sin^{m}\theta \sin^{m}\phi$$

The nominal value of ϕ was taken to be zero and the patterns were then modified to have the form

$$\bar{W}(\theta, 0) = \sum_{n} a'_{n} \cos^{n}\theta$$

with the coefficients

$$a'_{0} = a_{00} + .0173\, a_{20} + .0006\, a_{40} + .0172\, a_{02} + .0006(a_{22}+a_{04})$$

$$a'_{2} = .9434\, a_{20} + .0973\, a_{40} + .0084\, a_{60} + .0048\, a_{02} + .0160\, a_{22} + .0035\, a_{42} + .0005\, a_{04} + .0006\, a_{24}$$

$$a'_{4} = .8257\, a_{40} + .2161\, a_{60} + .0042\, a_{22} + .0155\, a_{42}$$

$$a'_{6} = .7637\, a_{60} - .0002\, a_{42}$$

IV. THEORY

After the necessary corrections to the experimental data have been made, comparison with theoretical predictions becomes possible. The theory of angular correlations has been presented in the literature [13, 14] and only a qualitative discussion of the pertinent formulae will be given here. Additional detail will be introduced, or at least emphasized, in the discussion of the experimental significance of the formulae.

1) The Angular Correlation Formula

The angular correlation experiments which were performed involved a nuclear reaction where alpha particles and associated gamma rays were detected following bombardment of a target nucleus with protons. This type of nuclear reaction is considered in three stages: first, a proton combines with a target nucleus to form a compound nucleus; the compound nucleus then emits an alpha particle leaving the residual nucleus in an excited state; finally, the residual nucleus decays to its ground state by gamma emission. Three directions require definition. The alpha particle is chosen to define a z-axis which makes an angle θ_a with the incident proton direction. The plane containing the alpha particle and the proton is taken to be the $\phi = 0$ plane. The direction of the gamma ray is then specified by the usual spherical coordinates θ, ϕ. These coordinates are all shown in Figure 18.

The differential cross section for emission of an alpha particle into a solid angle $d\Omega_a$ at θ_a and a gamma-ray into $d\Omega_\gamma$ at θ, ϕ when the proton bombarding energy is E_p is given by[2]

$$d\sigma(E_p, \theta_a, \theta, \phi) = \pi\lambda^2 \left| \sum_{r,s} \frac{\langle A|H_1|C_r\rangle\langle C_r|H_2|C_s\rangle\langle C_s|H_3|B\rangle}{E_p - E_r + \frac{1}{2}i\Gamma_r} \right|^2 d\Omega_a\, d\Omega_\gamma$$

where the numerator inside the modulus is a product of three matrix elements representing the formation of the compound nucleus, its subsequent breakup, and the gamma-ray emission. These matrix elements can then be resolved into an unknown factor depending on the specifically nuclear properties of the process and a transformation coefficient describing the combination of angular momenta.

Three angular correlation or angular distribution patterns arise in this particular situation. The (p-a) angular distribution pattern may be found by omitting the final matrix element. The (p-γ) angular distribution pattern is found by integrating over all possible directions of the alpha particle. The (a-γ) correlation pattern is given by the above formula directly. For the special case of alpha particle emission and a 0^+ final state in the residual nucleus, the angular correlation function is[2]

$$W(\theta,\phi) = \sum_s \sum_{m_s} \left| \sum_l \sum_{m_l} f_i(l) \langle s, m_s; l, m_l | j_1, m_1\rangle Y_l^{m_l}(\theta_a, 0) \times \sum_{l'} (2l'+1)^{1/2} f_e(l') \langle j_1, m_1 | l', 0; j_2, m_2\rangle \vec{X}_{j_2}^{m_2}(\theta,\phi) \right|^2$$

s = incoming channel spin

l = relative orbital angular momentum of the incident proton and the target nucleus

j_1 = spin of compound nucleus

j_2 = spin of excited state of residual nucleus

ℓ' = relative orbital angular momentum of alpha particle and excited residual nucleus

$\vec{X}^{m_2}_{J_2}(\theta,\phi)$ = γ-ray radiation function

The spin projections for the different spins are identified by their subscripts, e.g. m_s is the projection of the spin s. $f_i(\ell)$ and $f_e(\ell)$ are complex factors describing the probability amplitudes associated with the different orbital angular momenta.

A somewhat naive discussion might serve to clarify the events described in the correlation function. Consider a classical picture of a two particle system

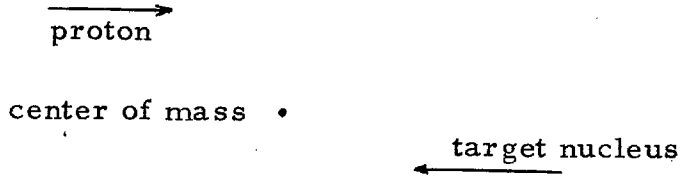

with its center of mass at rest and have the particles combine into a single particle which will then spin about the center of mass. The angular momentum of the final system may be simply related to the linear momentum and spins of the two particles and to the impact parameter and is not affected by the forces joining the two particles. In the angular correlation function, the forces involved in the formation of a compound nucleus have been separated from the geometrical implications of such a process and the Clebsch-Gordon coefficients $\langle\ \rangle$ relate the combination of two angular momentum vectors to form a third. This would arise in the classical sense if the particle were to break up into two particles which were spinning as they flew apart.

The classical picture also defines the angular momentum vector of the system to be at right angles to the particle direction and this accounts for $m_{\ell'} = 0$ in the angular correlation function

where the alpha particle direction has been chosen to be the z-axis. Choice of the proton direction to be the z-axis would have given $m_l = 0$ and the transformation of the proton wave function from a system of this type to one quantized along the alpha particle direction has introduced the terms $Y_l^{m_l}(\theta_a, 0)$.

2) Effect of Higher Orbital Angular Momenta

The angular correlation formula recognizes the possibility of higher orbital angular momenta of the proton and the alpha particle contributing significantly to the reaction. If the proton can have the orbital angular momenta values l and $l+2$ in forming the compound nucleus, then the relative amplitude of the two contributing waves is defined by A and the phase difference between the two waves is α. This gives the relation

$$\frac{f_i(l+2)}{f_i(l)} = A e^{i\alpha}$$

The phase shift, apart from an uncertainty of π, associated with the orbital angular momentum l in a Coulomb field, is given by[2]

$$\delta_l = -\tan \frac{F_l}{G_l} - \eta \log 2kR + \sigma_l - \frac{1}{2} l\pi$$

F_l, G_l are the regular and irregular solutions of the Coulomb wave equation; $\eta = \frac{Z_1 Z_2 e^2}{\hbar v}$; $k = \frac{\mu v}{\hbar}$, μ being the reduced mass of the system; R is the nuclear radius and $\sigma_l = \Gamma(l+1+i\eta)$. The interesting proton energies will lie well below the barrier

height so that $F_\ell << G_\ell$ and the phase difference between two waves of orbital angular momenta ℓ and $\ell+2$ becomes

$$\alpha = \delta_{\ell,\ell+2} = \tan^{-1}\frac{\eta}{\ell+2} + \tan^{-1}\frac{\eta}{\ell+1} - \pi$$

This value is calculated and its sign is considered to be undetermined in the evaluation of the experimental data.

A similar development applies to the alpha particles. The parameters defined in this case are

$$\frac{f_e(\ell'+2)}{f_e(\ell')} = Be^{i\beta}$$

and calculated values of $|\cos\beta|$ are used in evaluating the experiments.

3) Experimental Application of the Angular Correlation Formula

The three angles θ_a, θ, ϕ appearing in the angular correlation formula allow a number of possible experimental arrangements and the experimentalist is faced with the problem of choosing the most rewarding one. In order to do this, a criterion must be established.

The first requirement might be the retention of possible symmetries in the correlation pattern. This would have the advantage that deviations in these symmetries would result from some outside source, for example, faulty experimental geometry or interference with neighboring nuclear states. Another possible requirement is simplification of the expected correlation patterns. This requirement must be applied with caution so that it facilitates the analysis of experiments without removing the desired information. A final factor is, of course, the feasibility of the experiment in the laboratory.

An immediate restriction might be placed on the experiment

and this would require that only a single detector vary in space during the experiment. This restriction is convenient experimentally and simplifies the study of possible experimental arrangements. Two cases are to be considered; the alpha detector is to be kept fixed or the alpha detector is to rotate. A fixed alpha detector will be discussed first.

In order to retain possible symmetries in the correlation pattern, it is necessary to discuss the sources of asymmetry in the experiment which make an angular distribution or angular correlation pattern possible. The population of substates of a system with angular momentum J will refer to the different probabilities for the system having the different projections m_J, m_{J-1}, ... , $-m_J$. An isolated resonant state is considered. The incoming proton beam then defines a direction in the experiment and brings a spatial sense to the processes which occur. The orbital angular momentum of the protons is perpendicular to the proton direction so that the population of substates of the compound nucleus will be symmetric about $\theta_a = \frac{\pi}{2}$ and, of course, $\theta_a = 0$. A similar argument applies to the alpha particle so that the choice of $\theta_a = \frac{\pi}{2}$ or $\theta_a = 0$ for the alpha detector retains the possible symmetries. Another choice of θ_a gives terms of the form $A(\theta, \phi)\sin\theta\cos\theta\cos\phi$, similar to terms appearing for $\theta_a = \frac{\pi}{2}$ when two states of opposite parity overlap in the compound nucleus.

The choice of $\theta_a = 0$ gives a correlation pattern that can depend only on θ. This is easily seen because the two angles θ, ϕ require definition of a plane in space and the choice of $\theta_a = 0$ defines only a line. The primary disadvantage in this arrangement would be the limited range of values of θ because of the physical size of the

alpha detector and the proton beam tube.

Choice of $\theta_a = \frac{\pi}{2}$ leaves a further choice in the movement of the gamma detector which is a function of the two angles θ, ϕ. The three cases which appear to offer the most convenient experimental arrangement will be discussed. These are 1) $\phi = 0$, θ varying; 2) $\phi = \frac{\pi}{2}$, θ varying; 3) $\theta = \frac{\pi}{2}$, ϕ varying.

$\phi = 0$; θ varying. This is probably the simplest experimental arrangement. No simplification of the correlation pattern appears to occur, i.e. one might expect terms of the form $\cos^{\nu}\theta$ where $\nu \leq 2j_2$ with ν even. This is clearly the maximum possible complexity of an angular correlation pattern. A secondary disadvantage is the range of possible values of θ. The values of θ range over about 150° with the experimental arrangement that has been discussed earlier.

$\phi = \frac{\pi}{2}$; θ varying. The experimental arrangement for this case would be somewhat more complex than in the previous case. Correlation patterns which have been calculated in the course of this work appear to indicate that the complexity of the pattern is limited by both ℓ' and j_2, i.e. $\cos^{\nu}\theta$ terms would have $\nu \leq \mathrm{Min}(2\ell', 2j_2)$. The range of possible values of θ would be somewhat greater than in the first case and might be expected to be about 200° with the strong-focussing magnetic spectrometer.

$\theta = \frac{\pi}{2}$; ϕ varying. This experimental arrangement would be similar to the second case. The correlation pattern is a function of ϕ when the sum over m exists and cross-products of the radiation functions occur. Calculated patterns for this case appear to indicate that one might expect $\cos^{\nu}\phi$ terms with $\nu \leq \mathrm{Min}(2\ell, 2j_1, 2j_2)$.

The range of values of ϕ is limited only by the proton beam tube and is considerably larger than in the other two cases.

It is of some interest to note that the complexity rules, if correct, for the three cases differ in such a way as to convey a maximum amount of information. The choice of $\phi = 0$, for example, determines a maximum j_2. Case 2, where $\phi = \frac{\pi}{2}$, will then show whether $\ell' \leq j_2$, and, finally, $\theta = \frac{\pi}{2}$ with ϕ varying determines the minimum value between ℓ, j_1, and j_2.

If the alpha detector is allowed to rotate and the gamma detector is held fixed, then the correlation function given earlier is not satisfactory. The system must be transformed so that the proton direction or the gamma ray direction is the z-axis. Arguments similar to those given earlier then place the gamma detector at right angles to the proton beam and the rotation of the alpha detector may be discussed in a vein similar to that given for rotation of the gamma detector. This will not be done here because it was found more convenient experimentally to fix the position of the alpha detector.

The experimental arrangement which was used was the case where $\theta_a = \frac{\pi}{2}$, $\phi = 0$, and θ varied.

V. EXPERIMENTAL RESULTS

1) The Compound Nucleus Ne^{20}

Nuclear states of Ne^{20} are formed when F^{19} is bombarded with protons. These Ne^{20} states may then decay by alpha emission to the ground state or the lower excited states of the O^{16} nucleus. The ground state and the first excited, or pair-emitting, state of O^{16} at 6.05 Mev have the spin assignment 0^+ and alpha particles to these two states are denoted by α_o and α_π respectively. Alpha decay to these states in O^{16} can take place only from Ne^{20} states with spin J and parity $(-1)^J$.

The next three excited states of O^{16} at 6.14, 6.91, and 7.12 Mev have the spin assignments 3^-, 2^+, 1^- and alpha particle emission to any of these three states is followed by a gamma ray emission leaving the O^{16} in its ground state. The alpha particles to these three states of O^{16} are denoted by α_1, α_2, and α_3 respectively and all Ne^{20} states, except those with the assignment 0^-, might emit these alpha particles. In general, α_o and α_π-emitting states of Ne^{20} have not been found to coincide with the α_1, α_2, α_3-emitting states. Consequently, Ne^{20} states decaying by α_1, α_2, and α_3-emission might be expected to have spin J and parity $(-1)^{J+1}$. This is not considered a restriction in the analysis of the experiments.

Alternative modes of decay of the Ne^{20} compound nucleus which have been studied include the $F^{19}(p, p)F^{19}$, $F^{19}(p, p'\gamma)F^{19}$, and $F^{19}(p, \gamma)Ne^{20}$ reactions. In the elastic scattering of protons off F^{19}, the resonant states in Ne^{20} are observed as anomalies in the Rutherford scattering results. The interference between the

Coulomb scattering and the resonant scattering depends on terms like $P_l(\cos\theta)$ so that a study of the excitation curve of proton scattering at different angles is extremely helpful in determining the incoming proton orbital angular momenta. This work has been carried out by Webb[15] and provides strong evidence for the possible assignments of many of the Ne^{20} states mentioned here. In general, the elastic scattering experiments have been successful in eliminating a large number of possible assignments, but have required further experimental evidence to make a final choice of the assignment.

2) Experiments

The Ne^{20} states which were studied are reached by bombarding F^{19} with protons at the proton energies of 874, 935, 1280, 1346, and 1372 kev. The targets were in all cases, CaF_2 and, at the 874, 935, and 1372 kev resonances, the targets were about 10 kev thick to 1 Mev incident protons. The target used at the 1280 kev resonance was about 5 kev thick and the 1346 kev resonance was studied using a target less than 4 kev in thickness. The experiments were performed with the gamma detector in the $\phi = 0$ plane. Several points were also taken on the other side of $\theta = 180^\circ$ in the $\phi = 180^\circ$ plane. This distinction becomes important in the appearance of interference between different Ne^{20} states. The alpha detector was supposed to be placed at $\theta_a = 90^\circ$, but this was found to be in error on several of the experiments.

At most of the resonances, confirmation of the previous assignments was found and an attempt was made to evaluate the parameters A, B to give agreement with all of the existing data. Alpha-Gamma correlation experiments have been carried out by Seed and French[2]. Most of the alpha particle angular distributions have been measured

by Peterson[16] and angular distributions of the combined gamma-rays were measured by Day.[10] Finally, a partial separation of the gamma rays was made by Sanders[17] and the γ_1 angular distributions were measured by him at the 874, 935, and 1372 kev resonances.

E_p = 874 kev. The experimental (α_1, γ) correlation pattern is shown by the points in Figure 19. The experiment was performed with the alpha detector at 95° in the center of mass system and allowance for this has been made in the theoretical curve. A minimum of 1500 total coincidences were taken at each angle and, in the worst case, 67% of the total coincidences were true coincidences. One out of every three runs measured the accidental coincidence counting rate.

The large volume of experimental work on this level is in agreement with the assignment 2^-. The alternative assignment of 1^- given by the $F^{19}(p, p)F^{19}$ data is in particularly violent disagreement with the α_3 angular distributions measured by Peterson. The theoretical angular distribution patterns for the 2^- assignment are given in Appendix III. The parameters A, B and the signs of $\cos\alpha$ and $\cos\beta$ may also be determined for the different alpha particle groups.

The α_3 angular distribution depends only on the parameters A and $\cos\alpha$ and Peterson's work gave the values A = .06, $\cos\alpha$ = .438. The parameters B and $\cos\beta$ for the α_1-emission are involved in three experiments, the $(\alpha_1$-$\gamma)$ correlation pattern, Peterson's α_1 angular distribution, and Sanders' γ_1 angular distribution. Peterson's values of the parameters, B = 0.35, $\cos\beta$ = -.242, are inconsistent for the three experiments and the values chosen are B = 0.7,

$\cos\beta = .242$. The experimental and calculated α_1 and γ_1 angular distributions are

a. γ_1 angular distribution

Sanders: $I(\gamma_1) = 1 + (0 \pm .05)\cos^2\theta$

Calculated: $I(\gamma_1) = 1 - .05\cos^2\theta + .03\cos^4\theta$

b. α_1 angular distribution

Peterson: $I(\alpha_1) = 1 - .49\cos^2\theta$

Calculated: $I(\alpha_1) = 1 - .63\cos^2\theta + .04\cos^4\theta$

The α_1 angular distribution appears to be somewhat inconsistent. The angular correlation pattern shown in Figure 19 was measured in the $\phi = 0$ plane and is consistent with two sets of parameters, $B = 0.7$ $\cos\beta = .242$ or $B = 0.25$, $\cos\beta = -.242$. This correlation pattern was also measured by Seed and French[2] in the $\phi = \frac{\pi}{2}$ plane and they chose the parameters $B = 0.54$, $\cos\beta = -.242$. Their data is also consistent with the parameters $B = 0.7$, $\cos\beta = .242$ and these values were chosen.

Peterson's α_2 angular distribution and the $(\alpha_2$-$\gamma)$ correlation pattern by Seed and French are consistent with the parameters $B = 0.35$, $\cos\beta = -.250$ given by Seed and French. These values predict a gamma-ray angular distribution $I(\gamma_2) = 1 + 0.32\cos^2\theta$.

Finally, Chao et al.[18] have measured the relative yields of the three alpha particle groups at $\theta_2 = 138^\circ$. Peterson's angular distributions, combined with Chao's results, indicate the gamma ray intensities $I(\gamma_1) : I(\gamma_2) : I(\gamma_3)$ are in the ratio 12.6 : 5.9 : 1. The $\gamma_2 + \gamma_3$ angular distribution and the total gamma ray angular distribution may then be calculated and compared with experiment

c. $\gamma_2 + \gamma_3$ angular distribution

Sanders: $I(\gamma_2 + \gamma_3) = 1 + (.33 \pm .06)\cos^2\theta$

Calculated: $I(\gamma_2 + \gamma_3) = 1 + 0.36\cos^2\theta$

d. angular distribution

Day: $I(\gamma) = 1 + .11\cos^2\theta$

Calculated: $I(\gamma) = 1 + .10\cos^2\theta$

E_p = 935 kev. Figure 20 shows the experimental (α_1, γ) angular correlation points. The experiment was performed with the alpha detector at 90° in the center of mass system. A minimum of 1000 total coincidence counts were taken at each angle and more than 60% of the total coincidences were true coincidences. One-third of the runs were to measure the accidental coincidence counting rate.

A number of experiments have concurred in the assignment 1^+ for this level. A mixture of s- and d-wave protons may form this level, but no mixtures can occur for the three alpha particle groups. The calculated value $|\cos\alpha| = .033$ makes the experimental detection of d-wave protons improbable.

The anisotropy of the correlation pattern provided a check on the geometry of the experimental arrangement. The experimental points at $(\theta,\phi) = (165^\circ, 0^\circ)$ and $(\theta,\phi) = (165^\circ, 180^\circ)$ were studied and they were found to differ by about 15%. The formation of the Ne^{20} compound nucleus by s-wave protons must give a correlation pattern that is independent of ϕ and the asymmetry might then imply that the alpha detector is not set at the proper angle in the center of mass system. This was not found to be true and the asymmetry

was finally ascribed to interference effects with the 2^- state at 874 kev. As was pointed out by Dr. Christy, the choice of $\theta_a = 90^\circ$ meant that terms in $\cos\phi$ could appear in the correlation only by interference between two states of opposite parity. The coefficient of the interference pattern, which is related to the relative amplitudes of the two states was taken to be -.059. Simple Breit-Wigner calculations indicated a maximum value for this coefficient of .072.

E_p = 1280 kev. The experimental (α_1-γ) correlation points are shown in part (a) of Figure 21. The correlation pattern for an incident proton energy 30 kev below the resonance energy is shown in part (b) of the figure and much better statistics were obtained at this energy. Both of these patterns were obtained with the alpha detector at 95° in the center of mass system. Only 100 to 300 coincidence counts were obtained at each angle for the correlation pattern at 1280 kev, but the pattern was felt to be of some interest in determining the assignment of this level.

A broad resonance at 1189 kev[19] ($\Gamma \sim 110$ kev) overlaps the 1280 kev resonance and accounts for about 25% of the gamma rays observed here. The gamma rays from the 1189 kev resonance appear to be isotropic[10] and Day's measurement of the γ angular distribution at 1280 kev gave $I(\gamma) = 1 + 0.67\cos^2\theta$. This led Chao[20] to assign the 1280 kev resonance the spin and parity 3^+ and the angular correlation pattern agrees with this assignment. The theoretical 3^+ correlation pattern is shown in part (a) of Figure 21. The assignments 4^- and 5^+ are not excluded by the angular correlation pattern but the 5^+ assignment would give a large anisotropy in the gamma

ray angular distribution. The 1^- and 2^+ correlation patterns would have a maximum at $\theta = 180^\circ$ and these assignments appear to be excluded by the measured pattern.

E_p = 1346 kev. The experimental angular correlation points for the α_1-particle group are shown in Figure 22. Approximately 1000 coincidences were obtained at each angle. One-fifth of the runs measured the accidental coincidence counting rate.

No analysis of this data could be made. The large asymmetry about $\theta = 180^\circ$ is indicative of interference with a state of opposite parity, presumably the 1290 kev state. A further complication is introduced by the overlapping resonance at 1372 kev. An excitation curve of the gamma yield for the 1346 kev resonance is shown in Figure 23. The large background is due to the neighboring 1372 kev resonance.

Effects of the 1372 kev resonance are minimized by a study of the α_2 and α_3-particle groups. Peterson has done this work and obtained the assignment 2^- for the 1346 kev level and this is consistent with the proton elastic scattering. The total gamma ray angular distribution has been measured by Day to be $I(\gamma) = 1+0.233 \cos^2 \theta$. Peterson's and Day's work may be combined with Chao's measurements of the relative yields of alpha particles to predict the expected (α_1-γ) angular correlation pattern. This might be possible because of the 2^- assignment of the 1372 kev level. The experimental pattern is found by averaging out the interference effects. These two patterns are shown in Figure 22 and are in disagreement.

E_p = 1372 kev. Figure 24 shows the experimental (α_1-γ) angular correlation pattern. Once again, over 1000 total coincidences were obtained at each angle and 70°/o or more of these coincidences were true coincidences. One-fourth of the runs measured the accidental coincidence counting rate.

The proton elastic scattering by Webb indicated an assignment for this level of either 1^- or 2^-. Peterson measured the α_3 angular distribution as isotropic and this would favor a 1^- assignment. Sanders' measurement of the $\gamma_2 + \gamma_3$ angular distribution gave $I(\gamma_2+\gamma_3) = 1 + (.58 \pm .13)\cos^2\theta$ and this is inconsistent with the 1^- assignment. In an effort to resolve this disagreement, the α_3 angular distribution was checked at two angles $\theta_2 = 90^\circ$ and $\theta_2 = 157^\circ 30'$. The results of this check at the 1372 kev resonance and at the 935 and 1346 kev resonances is shown in Table 2.

Table 2

E_p	α_3 Intensities at $\theta_2 = 157^\circ 30'$ Normalized to $\theta_2 = 90^\circ$	
	Peterson's Work	Present Work
935 kev	1.0	.90
1346 kev	1.6	1.64
1372 kev	1.0	1.33

Disagreement with Peterson's work at the 1372 kev resonance was found.

For this reason, the assignment 2^- was preferred and the angular correlation pattern was fit with the parameters A = .05, $\cos\alpha$ = .605, B = 0.92, $\cos\beta$ = -.319. The predicted γ_1 angular

distribution may then be compared with Sanders' measured angular distribution

a. γ_1 angular distribution

Sanders: $I(\gamma_1) = 1 - (.14 \pm .03) \cos^2\theta$

Calculated: $I(\gamma_1) = 1 - .15 \cos^2\theta + .03 \cos^4\theta$

APPENDIX I

MOTION OF A PARTICLE IN A MAGNETIC FIELD

A magnetic field of the form

$$\vec{B} = \vec{e}_r B_0 \left[1 - n \frac{r - r_0}{r_0} \right] - \vec{e}_r B_0 n \frac{z}{r_0}$$

is considered. A cylindrical coordinate system r, ϕ, z is used and the motion of particles of mass m and charge q in the magnetic field is described. The value of B_0 is chosen so that the steady motion solutions of the equations of motion $(\vec{F} = q \vec{v} \times \vec{B})$ are

$$r = r_0 \qquad z = 0 \qquad \dot{\phi} = -\frac{q}{m} B_0 = -\omega_0$$

Introducing the variables

$$\rho = \frac{r - r_0}{r_0} \qquad z = \frac{z}{r_0}$$

and expressing these variables are functions of ϕ gives the two equations

$$\rho'' + (1-n)\rho = (2n-1)\rho^2 - \frac{1}{2}\rho'^2 - \frac{1}{2}z'^2$$

$$z'' + nz = -3\rho' z' - 2nz\rho$$

where terms of second order in z and ρ have been retained. Differentiation by ϕ is indicated. The linearized equations of motion are found by setting the second order terms equal to zero.

If $z = 0$ and $z' = 0$ the equation in ρ becomes

$$\rho'' + (1-n)\rho = (2n-1)\rho^2 - \frac{1}{2}\rho'^2$$

Take $n < 0$ and with an absolute value large compared to unity. An

approximate solution for ρ is $\qquad k = \sqrt{|n|}$

$$\rho = C\cos k\phi + \frac{B}{k}\sin k\phi + C^2\left[\cos k\phi + \frac{1}{4}\cos 2k\phi - \frac{5}{4}\right]$$
$$+ \frac{B^2}{k^2}\left[\frac{3}{2}\cos k\phi - \frac{1}{4}\cos 2k\phi - \frac{5}{4}\right] + \frac{BC}{k}\left[-\sin k\phi + \frac{1}{2}\sin 2k\phi\right]$$

The constants C and B are the same constants appearing in the first-order solution

$$\rho = C\cos k\phi + \frac{B}{k}\sin k\phi$$

For $n > 0$ the substitution $i\sqrt{n} = \sqrt{n}$ is made and the solution becomes

$$\rho = C\cosh k\phi + \frac{B}{k}\sinh k\phi + C^2\left[\frac{1}{4}\cosh 2k\phi + \cosh k\phi - \frac{5}{4}\right]$$
$$+ \frac{B^2}{k^2}\left[\frac{1}{4}\cosh 2k\phi - \frac{3}{2}\cosh k\phi + \frac{5}{4}\right] + \frac{BC}{k}\left[\frac{1}{2}\sinh 2k\phi - \sinh k\phi\right]$$

To obtain focussing in the $z = 0$ plane to the second-order, the path length in the second magnet is made a variable. Consider the arrangement where $n > 0$ in the first magnet and $n < 0$ in the second magnet. The path length in the second magnet is denoted by $k\phi = k\Phi + k\phi_1$. If $k\phi_1$ is taken to be small, and ρ_1 is the solution for the fixed length $k\Phi$, then $\rho = \rho_1 + k\phi_1$

$$\rho'/k = \rho_1'/k - k\phi_1\left[\rho_1 + \frac{5}{4}\left(A^2 + \frac{B^2}{k^2}\right) + \frac{3}{4}\left(A^2 - \frac{B^2}{k^2}\right)\cos 2k\phi - \frac{3}{2}A\frac{B}{k}\sin 2k\phi\right]$$

$$= \frac{\rho_1'}{k} - k\phi_1\left[\rho_1 + \alpha_1\right] \qquad (A = C)$$

These equations then define a1. If ρ_0 is the first-order solution for

the second magnet, then the following relations exist

$$kd_o = \frac{-\rho_o}{\rho_o'/k}$$

$$\rho_1 = \rho_o + x \qquad \frac{\rho_1'}{k} = \frac{\rho_o'}{k} + y$$

with the definitions

$$x = C^2\left[\frac{1}{4}\cos 2k\Phi + \cos k\Phi - \frac{5}{4}\right] + \frac{B^2}{k^2}\left[-\frac{1}{4}\cos 2k\Phi + \frac{3}{2}\cos k\Phi - \frac{5}{4}\right] + \frac{CB}{k}\left[\frac{1}{2}\sin 2k\Phi - \sin k\Phi\right]$$

$$y = -C^2\left[\frac{1}{2}\sin 2k\Phi + \sin k\Phi\right] + \frac{B^2}{k^2}\left[\frac{1}{2}\sin 2k\Phi - \frac{3}{2}\sin k\Phi\right] + \frac{BC}{k}\left[\cos 2k\Phi - \cos k\Phi\right]$$

Finally, in order to make $\rho = 0$ at the distance d_o beyond the second magnet, the relation

$$k\phi_1 = \frac{x - kd_o y}{\frac{\rho_o'}{k} - kd_o\rho_o + y - kd_o x - kd_o\alpha_1}$$

must be satisfied.

APPENDIX II

EFFECT OF COUNTER RESOLUTION ON CORRELATION FUNCTION

The finite solid angles of the radiation detectors made modifications of the theoretical angular correlation functions necessary for comparison with experimental measurements. The alpha detector is taken to be a line detector in a plane at right angles to the proton beam ($\theta_a = \frac{\pi}{2}$) so that all alpha particles that are accepted are at right angles to the incident proton direction. A theoretical angular correlation function of the form

$$W(\theta) = \sum_m a_{m_o} \cos^m \theta$$

is first considered, and, later, a function depending on the two angles θ, ϕ' is discussed. The gamma detector is a right circular cylinder with its base oriented towards the source and is considered uniformly sensitive out to a definite radius and insensitive beyond that radius. The measured correlation function is then

$$\bar{W}(\theta) = \frac{1}{\Omega_\alpha \Omega_\gamma} \int d\Omega_\alpha \, d\Omega_\gamma \, W(\theta')$$

$$d\Omega_\alpha = \frac{2a}{b} \sqrt{\tan^2 \alpha_{max} - \tan^2 \alpha} \, d\alpha \qquad -\alpha_{max} \leq \alpha \leq \alpha_{max}$$

$$d\Omega_\gamma = \sin\beta \, d\beta \, d\phi \qquad 0 \leq \beta \leq \beta_{max} \qquad 0 \leq \phi \leq 2\pi$$

All of these angles appear in Figure A on the following page. a and b are the minor and major axes of the elliptical slit that defines the alpha detector solid angle.

The first substitution to be made is

$$\cos\theta' = \cos\theta'' \cos\alpha - \sin\alpha \sin\beta \sin\phi$$

and the correlation function then becomes

$$\bar{W}(\theta) = \sum_m a_{mo} \sum_k (-1)^k \binom{m}{k} Q_{mk} \frac{1}{\Omega_\gamma} \int d\Omega_\gamma \cos^{m-k}\theta'' \sin^k\phi \sin^k\beta$$

where the integral over the alpha detector solid angle has been defined

$$Q_{mk} = \frac{1}{\Omega_\alpha} \int \cos^{m-k}\alpha \sin^k\alpha \, d\alpha$$

Now the substitution

$$\cos\theta'' = \cos\theta\cos\beta + \sin\theta\sin\beta\cos\phi$$

gives a correlation function of the form

$$\bar{W}(\theta) = \sum_m a_{mo} \sum_k (-1)^k \binom{m}{k} Q_{mk} \sum_r \binom{m-k}{r} \cos^{m-k-r}\theta \sin^r\theta$$

$$\times \frac{1}{\Omega_\gamma} \int d\Omega_\gamma \cos^{m-k-r}\beta \sin^{k+r}\beta \sin^k\phi \cos^r\phi$$

Finally, defining the integrals

$$R_{mkr} = \frac{2\pi}{\Omega_\gamma} \int_0^{\beta_{max}} \cos^{m-k-r}\beta \sin^{k+r+1}\beta \, d\beta$$

$$S_{kr} = \frac{1}{2\pi} \int_0^{2\pi} \sin^k\phi \cos^r\phi \, d\phi$$

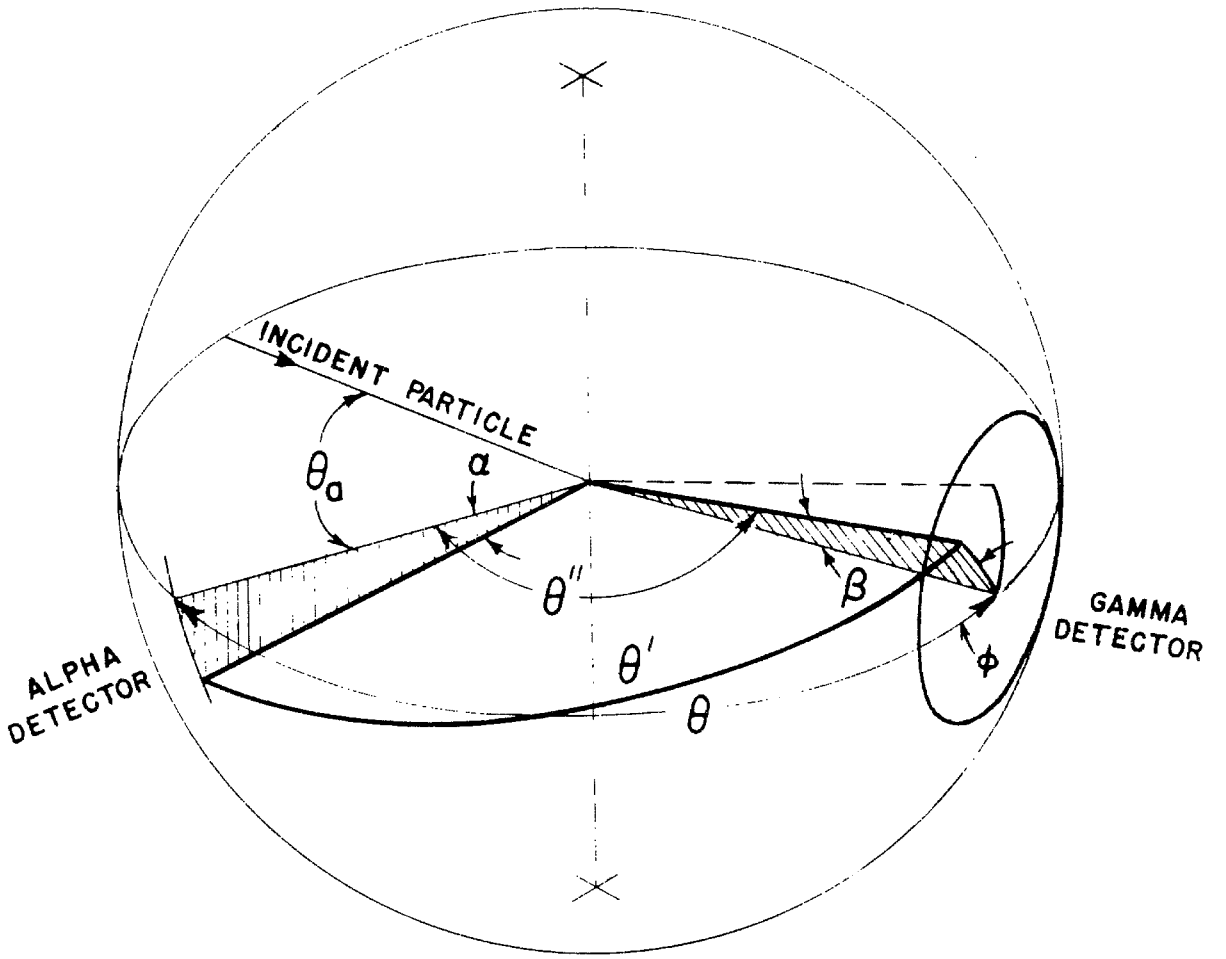
INCIDENT PARTICLE
θ_a
α
θ''
β
θ'
θ
ϕ
ALPHA DETECTOR
GAMMA DETECTOR

FIG.(A)

gives a final expression for the measured angular correlation function

$$\bar{W}(\theta) = \sum_{m,k,r} a_{mo} (-1)^k \binom{m}{k}\binom{m-k}{r} Q_{mk} R_{mkr} S_{kr} \cos^{m-k-r}\theta \sin^r\theta$$

The integrals are evaluated by placing them in the following forms

$$Q_{mk} = \frac{4\frac{a}{b}}{\Omega_\alpha \cos\alpha_{max}} \int_0^{y_1=\sin\alpha_{max}} \frac{(1-y^2)^{\frac{m-k}{2}} y^k}{\sqrt{y_1^2-y^2}\,(1-y^2)}\, dy \qquad (k \text{ even})$$

$$R_{mkr} = \frac{2\pi}{\Omega_\gamma} \int_{y_2=\cos\beta_{max}}^{1} y^{m-k-r} (1-y^2)^{\frac{k+r}{2}}\, dy$$

Finally, in order that S_{kr} be non zero when k is even, it is necessary that r be even and S_{kr} can then be written as a sum of integrals of the following form

$$\frac{2}{\pi}\int_0^{\frac{\pi}{2}} \sin^n\phi\, d\phi = \frac{2}{\pi}\int_0^{\frac{\pi}{2}} \cos^n\phi\, d\phi = \frac{1.3.5\cdots(n-1)}{2.4.6.\cdots n} \qquad (n \text{ even})$$

A correlation function depending on the two angles θ, ϕ' is considered next. The gamma detector rotates in the horizontal plane so that the nominal value of ϕ' is zero and the point to point geometry of Figure A gives

$$\cos\phi' = \frac{\sin\theta''}{\sin\theta'} \sin\left[\cos^{-1} - \frac{\sin\beta\sin\phi}{\sin\theta''}\right]$$

$$= \frac{1}{\sin\theta'}\left[\sin^2\theta'' - \sin^2\beta\sin^2\phi\right]^{\frac{1}{2}}$$

This can be written

$$\sin^2\theta' \sin^2\phi' = \cos^2\theta'' - \cos^2\theta' + \sin^2\beta \sin^2\phi$$

In order to facilitate use of the expression for ϕ', the theoretical correlation function is written

$$W(\theta,\phi') = \sum_{m,n} a_{mn} \cos^m\theta \sin^n\theta \sin^n\phi'$$

The discussion is simplified by taking n = 2. The measured correlation function is then

$$\bar{W}(\theta,o) = \frac{1}{\Omega_\alpha \Omega_\gamma} \int d\Omega_\alpha d\Omega_\gamma W(\theta',\phi')$$

and has the final form

$$\bar{W}(\theta,o) = \bar{W}(\theta) + \sum_m \sum_{K=0}^{m} \sum_{r=o}^{m+2-K} a_{m2} (-1)^K \binom{m}{K}\binom{m+2-k}{r} Q_{mK} R_{m+2,Kr} S_{Kr} \cos^{m+2-k-r}\theta \sin^r\theta$$

$$- \sum_m \sum_{K=0}^{m+2} \sum_{r=o}^{m+2-K} a_{m2} (-1)^K \binom{m+2}{K}\binom{m+2-k}{r} Q_{m+2,K} R_{m+2,Kr} S_{Kr} \cos^{m+2-k-r}\theta \sin^r\theta$$

$$+ \sum_m \sum_{K=0}^{m} \sum_{r=o}^{m+K} a_{m2} (-1) \binom{m}{K}\binom{m-k}{r} Q_{mk} \left[R_{mKr} - R_{m+2,Kr} \right] S_{K+2,r} \cos^{m-k-r}\theta \sin^r\theta$$

APPENDIX III

TABLE OF ANGULAR DISTRIBUTION AND ANGULAR CORRELATION FUNCTIONS

The distributions are for the different states in Ne^{20}. The subscripts 1, 2, 3 (e.g. a_1, a_2, a_3) refer to the first three gamma-emitting states of O^{16} which have the assignments 3^-, 2^+, 1^-. The parameters A, B, α, β have been defined in the text. Higher orbital angular momenta have not been considered in all cases. All correlation functions are given for $\theta_a = \frac{\pi}{2}$. A number of these distributions appear in Reference 2.

(The substitution $x = \cos\theta$ has been made.)

0^+ State in Ne^{20}

$(a_1\text{-}\gamma)$ $\quad 1 - 11x^2 + 35x^4 - 25x^6$

All alpha and gamma distributions are isotropic

1^+ State in Ne^{20}

$(p\text{-}a_1)$ $\quad 1 + \frac{1}{\sqrt{2}} A \cos\alpha\,(3x^2-1) + \frac{1}{4}A^2\,(5-3x^2)$

$(p\text{-}\gamma_1)$ $\quad 1 + \frac{3}{4\sqrt{2}} A \cos\alpha\,(3x^2-1) + \frac{1}{16}A^2\,(19-9x^2)$

$(p\text{-}a_2)$ $\quad 1 + \frac{1}{\sqrt{2}} A \cos\alpha\,(3x^2-1) + \frac{1}{4}A^2\,(5-3x^2)$

$(p\text{-}\gamma_2)$ $\quad 1 + \frac{1}{2\sqrt{2}} A \cos\alpha\,(3x^2-1) + \frac{1}{4}A^2\,(5-3x^2)$

$(p\text{-}a_3)$ $\quad 1 + \frac{1}{\sqrt{2}} A \cos\alpha\,(3x^2-1) + \frac{1}{4}A^2\,(5-3x^2)$

$(p\text{-}\gamma_3)$ $\quad 1 + \frac{1}{2\sqrt{2}} A \cos\alpha\,(1-3x^2) + \frac{1}{8}A^2\,(7+3x^2)$

$(a_1\text{-}\gamma)$ $\quad 1 + 111x^2 - 305x^4 + 225x^6$

$$- \frac{1}{2\sqrt{2}} A\cos\alpha \;\; 5-171x^2+455x^4-225x^6+6(1-x^2)\sin^2\phi(1-130x^2+225x^4)$$

$$+ \frac{1}{2}A^2 \;\; 4+81x^2-230x^4+225x^6-3(1-x^2)\sin^2\phi(1-130x^2+225x^4)$$

1^- State in Ne^{20} (Channel Spin 1^+)

$(p\text{-}\gamma_1)$ $\quad 1 - \frac{9}{23}x^2 + \frac{5}{92}B^2\,(17-3x^2)$

$(p\text{-}a_2)$ $\quad 1 - \frac{1}{7}x^2 + \frac{6}{7}\sqrt{\frac{2}{3}}\,B\cos\beta\,(3x^2-1) + \frac{4}{7}B^2\,(2-x^2)$

$(p\text{-}\gamma_2)$ $\quad 1 - \frac{1}{3}x^2 + \frac{2}{63}B^2\,(29-3x^2)$

$(p\text{-}a_3)$ $\quad 1 + \frac{1}{\sqrt{2}}\,B\cos\beta\,(3x^2-1) + \frac{1}{4}B^2\,(5-3x^2)$

$(p\text{-}\gamma_3)$ $\quad 1 + x^2 + \frac{1}{10}B^2\,(13+x^2)$

$(a_1\text{-}\gamma)$ $\quad 10 - 109x^2 + 340x^4 - 225x^6$

$$+ \sqrt{\frac{5}{3}}\,B\cos\beta \;\; 11 - 122x^2 + 395x^4 - 300x^6$$

$$+ \frac{5}{12}B^2 \;\; 17 - 186x^2 + 585x^4 - 400x^6 \qquad (\phi = 0)$$

1^- State in Ne^{20} (Channel Spin 0^+)

$-(p\text{-}\gamma_1)$ $\quad 1 + \frac{9}{7}x^2 + \frac{5}{28}B^2\,(7+3x^2)$

$(p\text{-}a_2)$ $\quad 1 + \frac{1}{3}x^2 + 2\sqrt{\frac{2}{3}}\,B\cos\beta\,(1-3x^2) + \frac{2}{3}B^2\,(1+2x^2)$

$(p\text{-}\gamma_2)$ $\quad 1 + x^2 + \frac{2}{3}B^2\,(1+3x^2)$

$(p\text{-}a_3)$ $\quad 1 + \sqrt{2}\,B\cos\beta\,(1-3x^2) + \frac{1}{2}B^2\,(1+3x^2)$

$(p\text{-}\gamma_3)$ $\quad 1 - x^2 + \frac{1}{10}B^2\,(7-x^2)$

$(a_1\text{-}\gamma)$ $\quad 1 - 10x^2 + 25x^4 + \frac{5}{12}B^2\,(101x^2-280x^4+225x^6) \qquad (\phi = 0)$

2^- State in Ne^{20}

$(p\text{-}a_1)$ $\quad 1 - \frac{2}{3}x^2 + \frac{1}{3}\sqrt{\frac{5}{2}}\,B\cos\beta\,(1-3x^2) + \frac{1}{72}B^2\,(55+3x^2)$

$$+ \frac{1}{6\sqrt{6}}\,A\cos\alpha\,(-1-6x^2+15x^4) + 4\sqrt{\frac{5}{2}}\,B\cos\beta\,(-3+24x^2-25x^4)$$

$$+ 2B^2\,(4-39x^2+45x^4)$$

$$+ \frac{1}{72}A^2\,(73-42x^2-15x^4) + 4\sqrt{\frac{5}{2}}\,B\cos\beta\,(9-42x^2+25x^4)$$

$$+ 2B^2\,(23+42x^2-45x^4)$$

$(p\text{-}\gamma_1)$ $\quad 1 + \frac{9}{37}x^2 + \frac{5}{74}B^2\,(19-9x^2)$

$$+ \frac{3}{37}\sqrt{\frac{2}{3}}\,A\cos\alpha\,(3-24x^2+25x^4) + \frac{5}{9}B^2\,(-3+3x^2+10x^4)$$

$$+ \frac{1}{74}A^2\,(71+42x^2-25x^4) + \frac{10}{9}B^2(87-42x^2-5x^4)$$

$(p\text{-}a_2)$ $1 - \frac{7}{9}x^2 + \frac{4}{9}B\cos\beta\,(1-3x^2) + \frac{2}{9}B^2\,(3 + x^2)$

$+ \frac{2}{9}\sqrt{\frac{2}{3}}\,A\cos\alpha\,\,(3x^2-1) + 2B\cos\beta(-3 + 24x^2 - 25x^4)$

$+ \frac{1}{2}B^2\,(7 - 66x^2 + 75x^4)$

$+ \frac{4}{27}A^2\,\,6-3x^2 + \frac{1}{14}B\cos\beta\,(63-354x^2 + 175x^4)$

$+ \frac{1}{8}B^2\,(29 + 78x^2 - 75x^4)$

$(p\text{-}\gamma_2)$ $1 + \frac{3}{7}x^2 + \frac{8}{49}B^2\,(8-3x^2)$

$+ \frac{2}{7}\sqrt{\frac{2}{3}}\,A\cos\alpha\,\,(-3 + 33x^2 - 40x^4) + \frac{6}{7}B^2\,(-1+6x^2-5x^4)$

$+ \frac{8}{7}A^2\,\,1 - x^2 + \frac{5}{3}x^4 + \frac{1}{98}B^2\,(117 - 78x^2 + 35x^4)$

$(p\text{-}a_3)$ $1 + x^2 + 2\sqrt{\frac{2}{3}}\,A\cos\alpha\,(1-9x^2+10x^4) + \frac{2}{3}A^2\,(1 + 6x^2-5x^4)$

$(p\text{-}\gamma_3)$ $1 + \frac{7}{11}x^2 + \frac{2}{11}\sqrt{\frac{2}{3}}\,A\cos\alpha\,(3x^2-1) + \frac{8}{33}A^2\,(4 + 3x^2)$

$(a_1\text{-}\gamma)$ $26-85x^2 + 300x^4 - 225x^6 + \sin^2\theta\sin^2\phi(-1+130x^2-225x^4)$

$+ \sqrt{10}\,B\cos\beta\,\,9-20x^2+85x^4-90x^6 - \sin^2\theta\,\sin^2\phi(-1+130x^2-225x^4$

$$+\frac{5}{2}B^2\ \ 5-22x^2+69x^4-36x^6+\sin^2\theta\sin^2\phi(-1+130x^2-225x^4)$$

$$+\sqrt{\frac{2}{3}}A\cos\alpha\ \ 52-670x^2+1100x^4-450x^6$$

$$+2\sin^2\theta\sin^2\phi\ (-251+2630x^2-2475x^4)$$

$$-50\sin^4\theta\sin^4\phi\ (-10+90x^2)$$

$$+2\sqrt{10}B\cos\beta\ \ 9-120x^2+185x^4-90x^6$$

$$+3\sin^2\theta\sin^2\phi\ \ (-33+290x^2-225x^4)$$

$$-10\sin^4\theta\sin^4\phi+(-10+90x^2)$$

$$+5B^2\ \ 5-62x^2+109x^4-36x^6$$

$$+4\sin^2\theta\sin^2\phi\ (-41+530x^2-585x^4)$$

$$-4\sin^4\theta\sin^4\phi\ (-10+90x^2)$$

$$+\frac{2}{3}A^2\ \ 26+40x^2+175x^4-225x^6$$

$$+16\sin^2\theta\sin^2\phi\ (31-280x^2+225x^4)$$

$$+50\sin^4\theta\sin^4\phi\ (-10+90x^2)$$

$$+ \sqrt{\frac{10}{2}} B\cos\beta \quad 9 + 30x^2 + 35x^4 - 90x^6$$

$$+ \sin^2\theta\sin^2\phi\ (51-630x^2 + 675x^4)$$

$$+ 5\ \sin^4\theta\ \sin^4\phi\ (-10 + 90x^2)$$

$$+ \frac{25}{2}B^2 \quad 5 - 2x^2 + 49x^4 - 36x^6$$

$$+ \sin^2\theta\ \sin^2\phi\ (19 - 70x^2 - 45x^4)$$

$$+ 2\ \sin^4\theta\ \sin^4\phi\ \ (-10 + 90x^2)$$

3^+ State in Ne^{20}

$(p\text{-}\gamma_1) \quad 1 + \frac{74}{75}x^2 - \frac{7}{45}x^4$

$(a_1\text{-}\gamma) \quad 1 - \frac{116}{845}x^2 - \frac{321}{169}x^4 + \frac{180}{169}x^4 \qquad (\phi = 0)$

4^- State in Ne^{20}

$(p\text{-}\gamma_1) \quad 83434 - 44475x^2 + 298305x^4 - 202125x^6$

$(a_1\text{-}\gamma) \quad 46 - 186x^2 + 239x^4 - 90x^6 \qquad (\phi = 0)$

5^+ State in Ne^{20}

$(p\text{-}\gamma_1) \quad 976 + 7871x^2 - 17010x^4 + 19635x^6$

$(a_1\text{-}\gamma) \quad 800 - 341x^2 - 1108x^4 + 858x^6$

REFERENCES

1. Barnes, French, and Devons, Nature, 166, 145 (1950)
2. J. Seed and A. P. French, Phys. Rev., 88, 1007 (1952)
3. Svartholm and Seigbahn, Ark. f Nat. Astr. o. Fys. 33A, No. 21 (1946)
4. Snyder, Lauritsen, Fowler, and Rubin, Phys. Rev., 74, 1564 (1948)
5. Courant, Livingston, and Snyder, Phys. Rev. 88, 1190 (1952)
6. C. A. Barnes, Phys. Rev., 97, 1226 (1955)
7. R. M. Sternheimer. Rev. Sci. Instr. 21, 213 (1953)
8. D. L. Judd, Rev. Sci. Instr., 21, 213 (1950)
9. R. M. L. Haver, Rev. Sci. Instr., 21, 750 (1950)
10. R. B. Day, Ph.D. Thesis, California Institute of Technology (1951)
11. M. E. Rose, Phys. Rev., 91, 610 (1953)
12. A. M. Feingold and S. Frankel, Phys. Rev., 97, 1025 (1955)
13. A. A. Kraus, Ph.D. Thesis, California Institute of Technology (1953)
14. L. C. Beidenham and M. E. Rose, Revs. Mod. Phys., 25, 729 (1953)
15. T. S. Webb, Ph.D. Thesis, California Institute of Technology (1955)
16. R. W. Peterson, Phys. Rev., 96, 1250 (1954)
17. J. E. Sanders, Phil. Mag. 43, 630 (1952); Phil. Mag. 44 1302 (1953)
18. Chao, Tollestrup, Fowler, and Lauritsen, Phys. Rev. 79, 108 (1950)
19. S. E. Hunt and K. Firth, Proc. Phys. Soc. (to be published)
20. C. Y. Chao, Phys. Rev. 80, 1035 (1950)

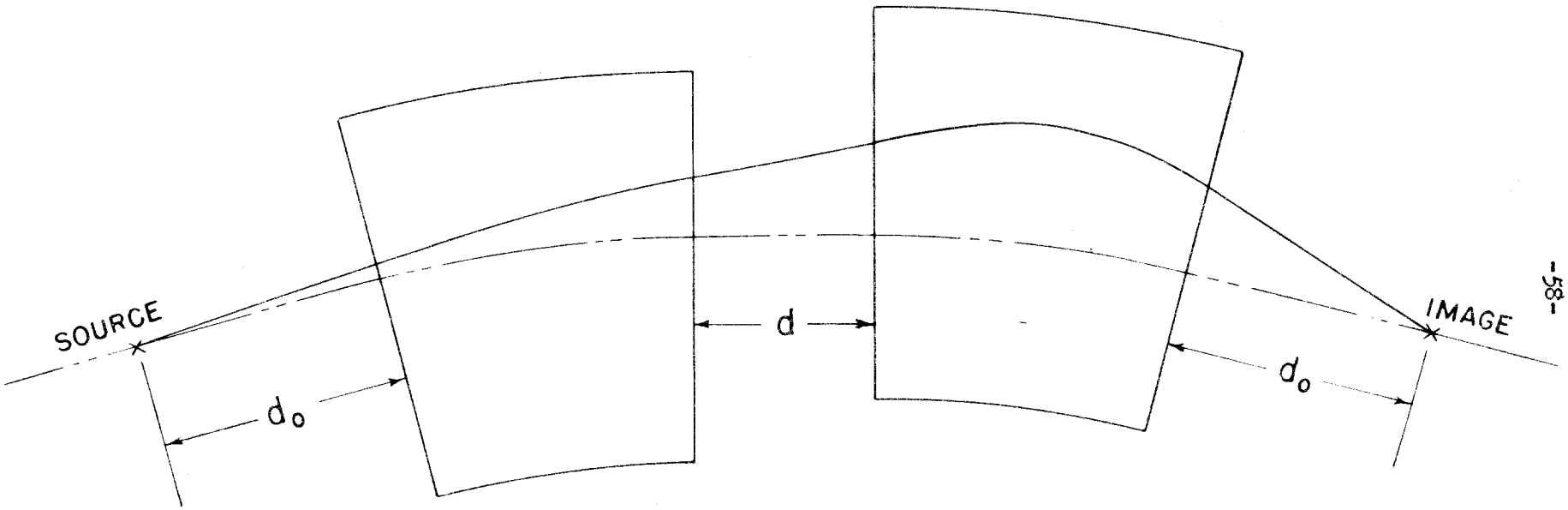

DOUBLE LENS STRONG-FOCUSSING
MAGNETIC SPECTROMETER

FIG. 1

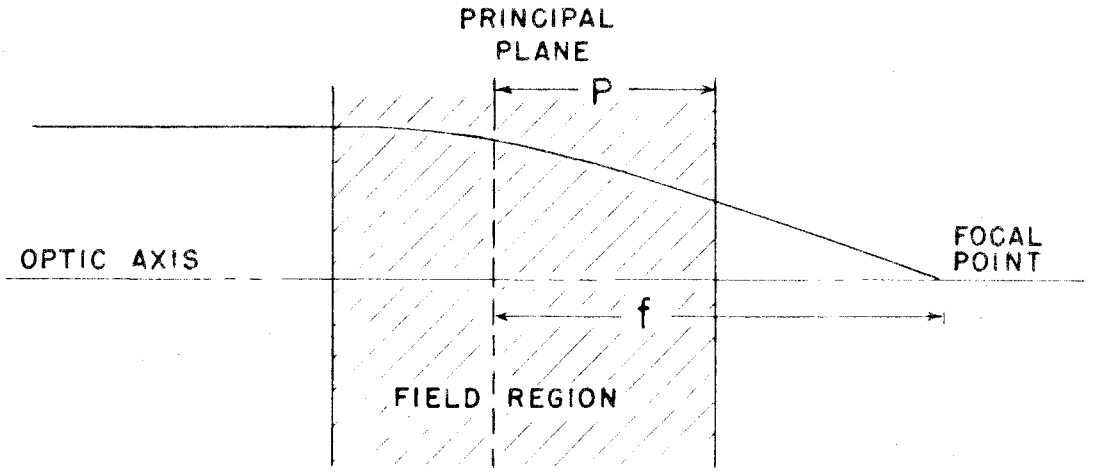

FIG.2 LOCATION OF PRINCIPAL PLANE AND FOCAL POINT OF SINGLE MAGNETIC LENS

(a) DIVERGENT-CONVERGENT CASE

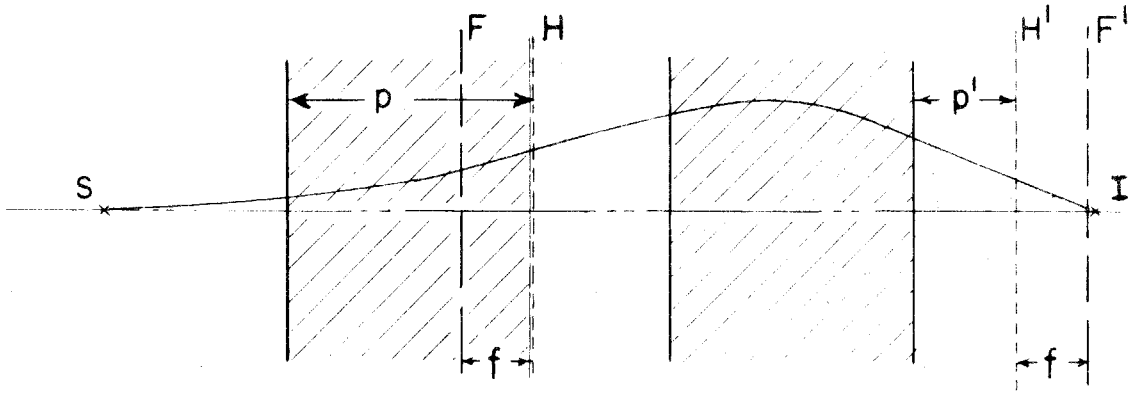

(b) CONVERGENT-DIVERGENT CASE

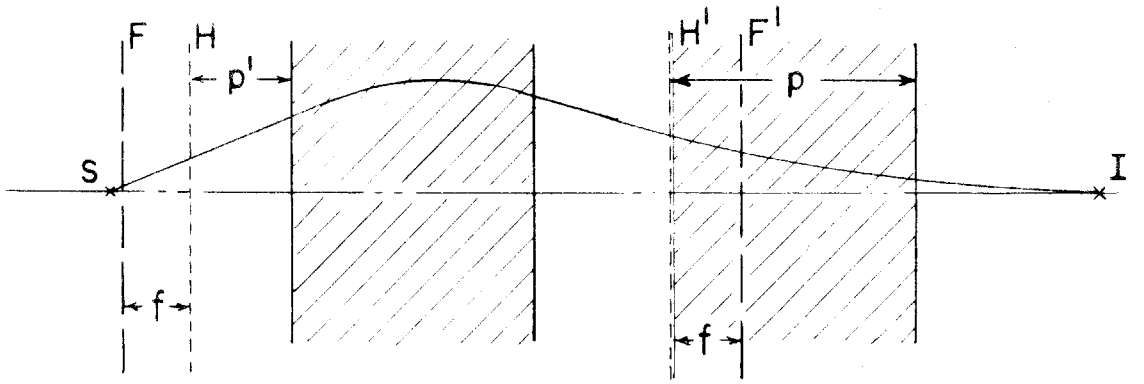

FIG.3 LOCATION OF PRINCIPAL PLANES AND FOCAL PLANES OF DOUBLE MAGNETIC LENS

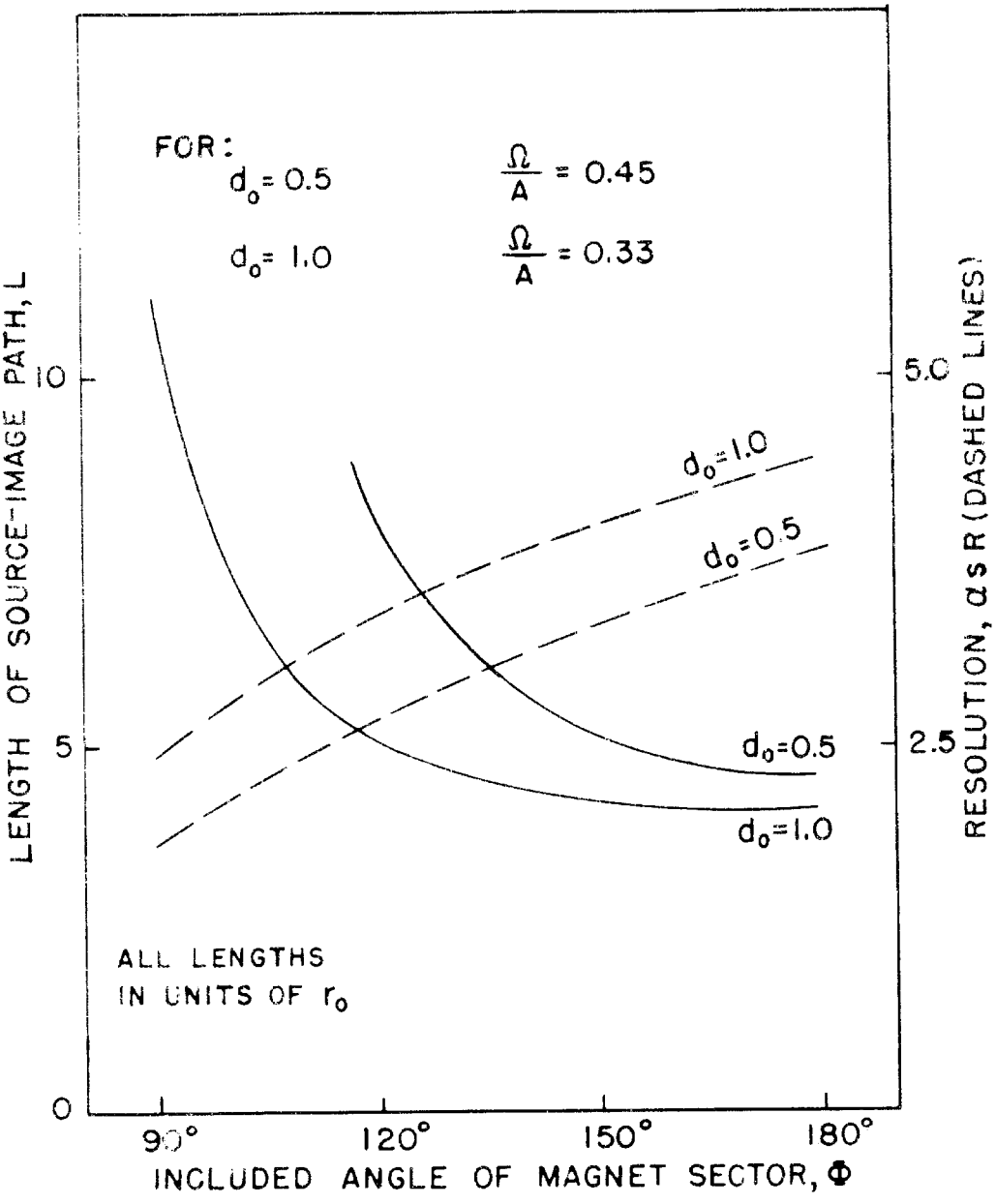

CHARACTERISTICS OF DOUBLE-FOCUSSING SPECTROMETER WITH n=0.5

FIG. 4

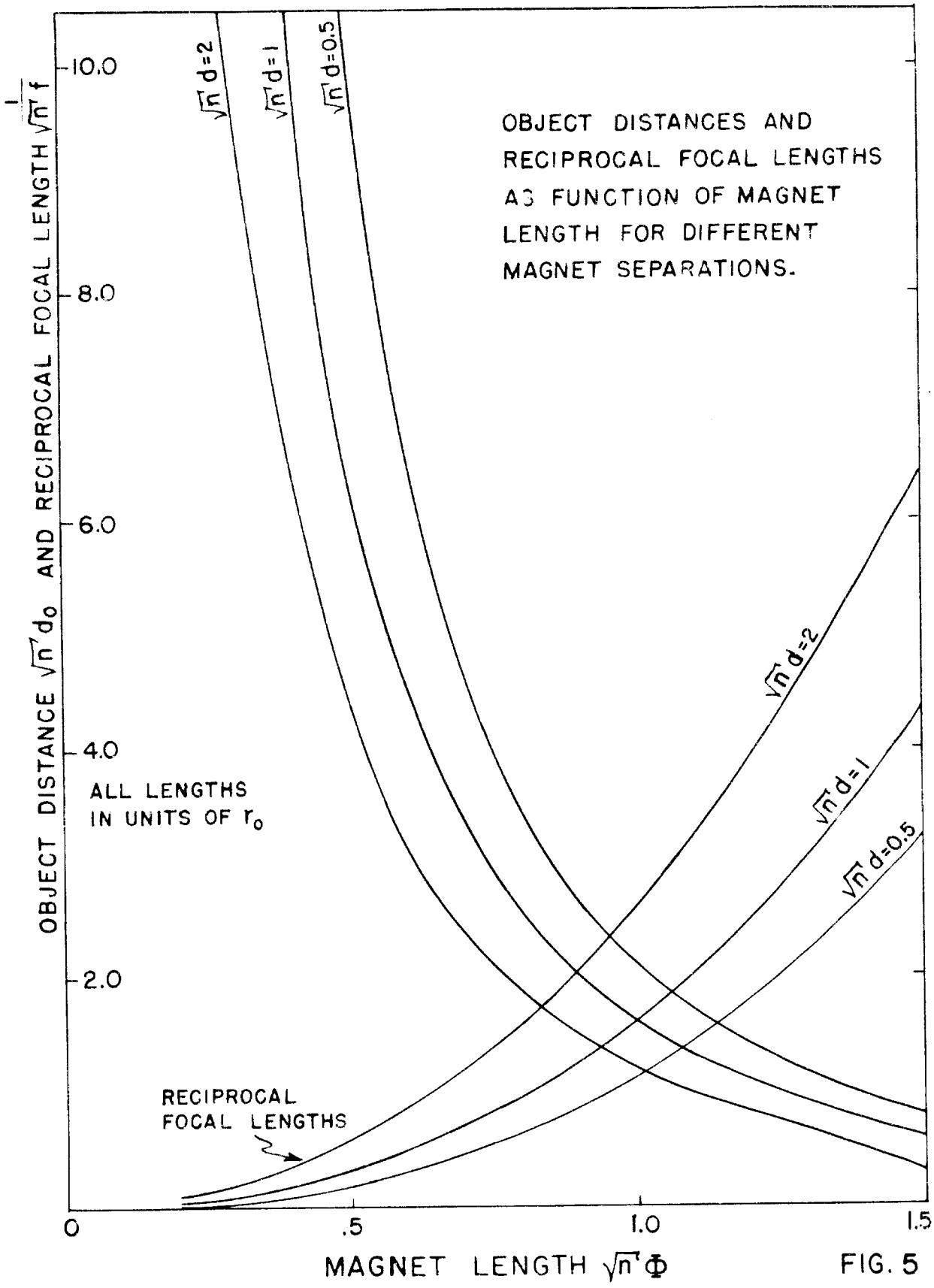
OBJECT DISTANCES AND RECIPROCAL FOCAL LENGTHS AS FUNCTION OF MAGNET LENGTH FOR DIFFERENT MAGNET SEPARATIONS.
OBJECT DISTANCE $\sqrt{n'}d_o$ AND RECIPROCAL FOCAL LENGTH $\frac{1}{\sqrt{n'}f}$
MAGNET LENGTH $\sqrt{n'}\Phi$
$\sqrt{n'}d=2$
$\sqrt{n'}d=1$
$\sqrt{n'}d=0.5$
ALL LENGTHS IN UNITS OF r_o
RECIPROCAL FOCAL LENGTHS
10.0
8.0
6.0
4.0
2.0
0
.5
1.0
1.5

FIG. 5

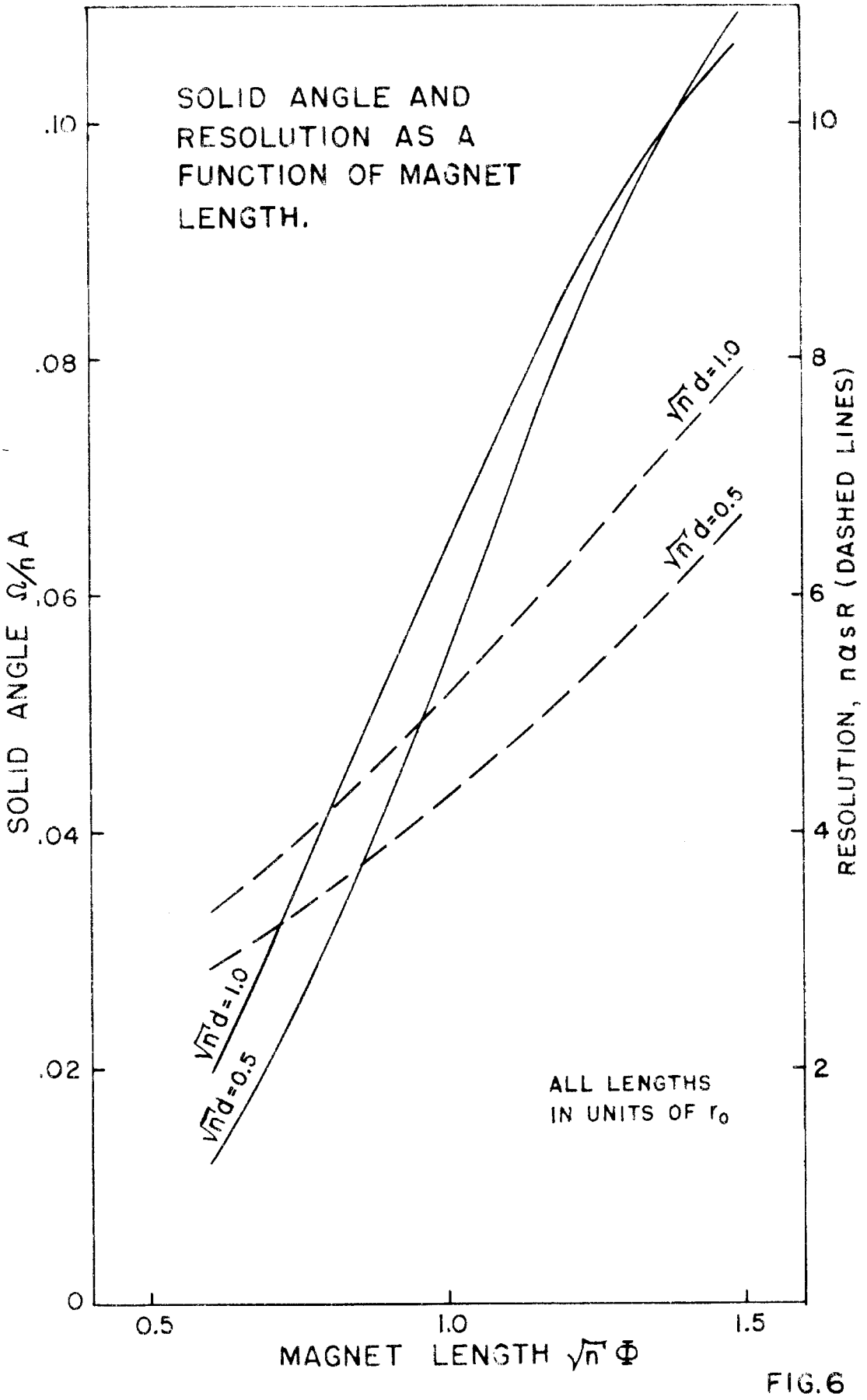
SOLID ANGLE AND
RESOLUTION AS A
FUNCTION OF MAGNET
LENGTH.
SOLID ANGLE Ω/n A
RESOLUTION, nαsR (DASHED LINES)
MAGNET LENGTH √n Φ
√n d=1.0
√n d=0.5
√n d=1.0
√n d=0.5
ALL LENGTHS
IN UNITS OF r0
.10
.08
.06
.04
.02
0
10
8
6
4
2
0.5
1.0
1.5

FIG.6

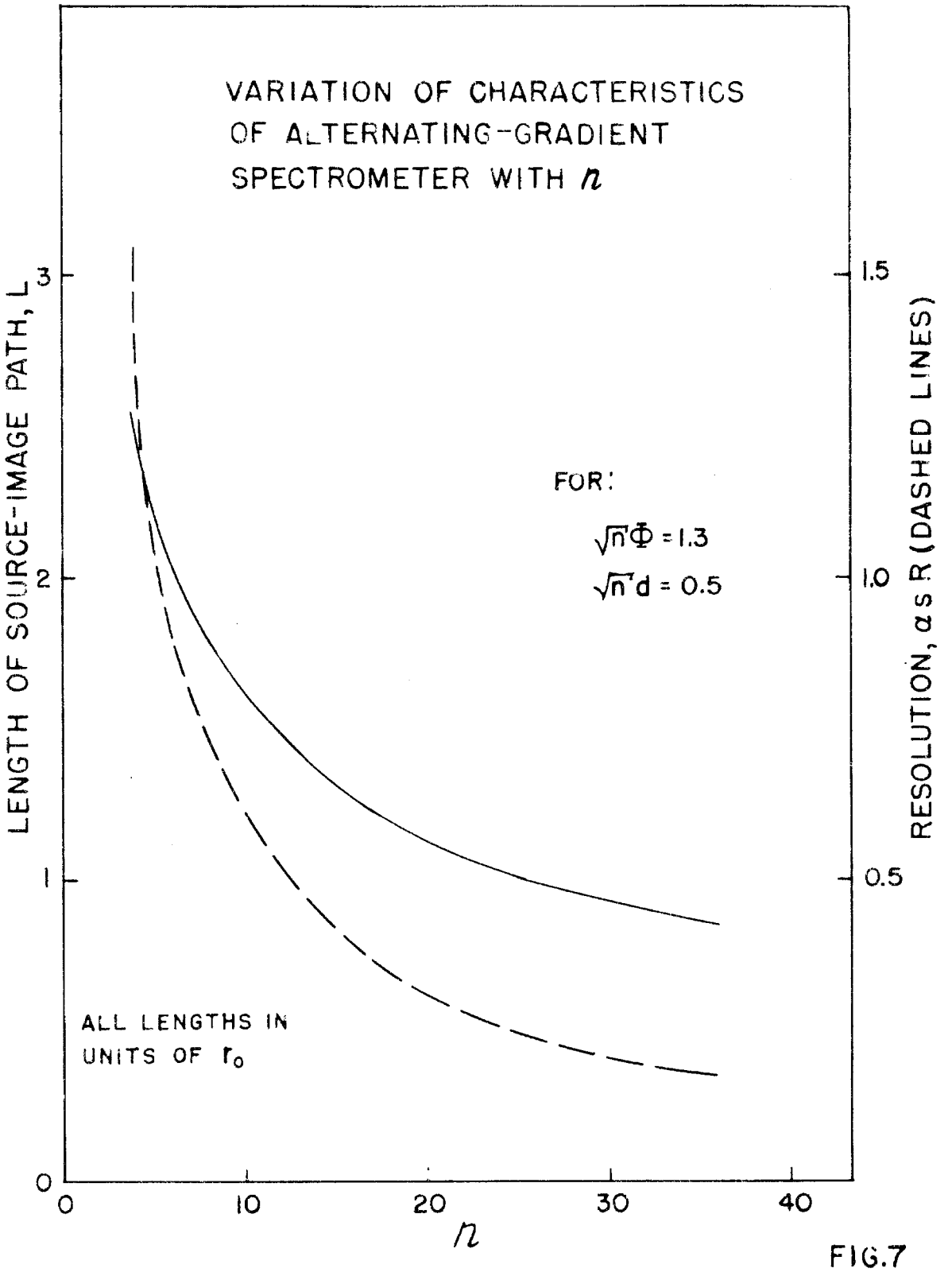
VARIATION OF CHARACTERISTICS
OF ALTERNATING-GRADIENT
SPECTROMETER WITH n
FOR:
$\sqrt{n'}\Phi = 1.3$
$\sqrt{n'}d = 0.5$
ALL LENGTHS IN
UNITS OF r_0
LENGTH OF SOURCE-IMAGE PATH, L
RESOLUTION, α s R (DASHED LINES)
n
0
10
20
30
40
1
2
3
0.5
1.0
1.5

FIG.7

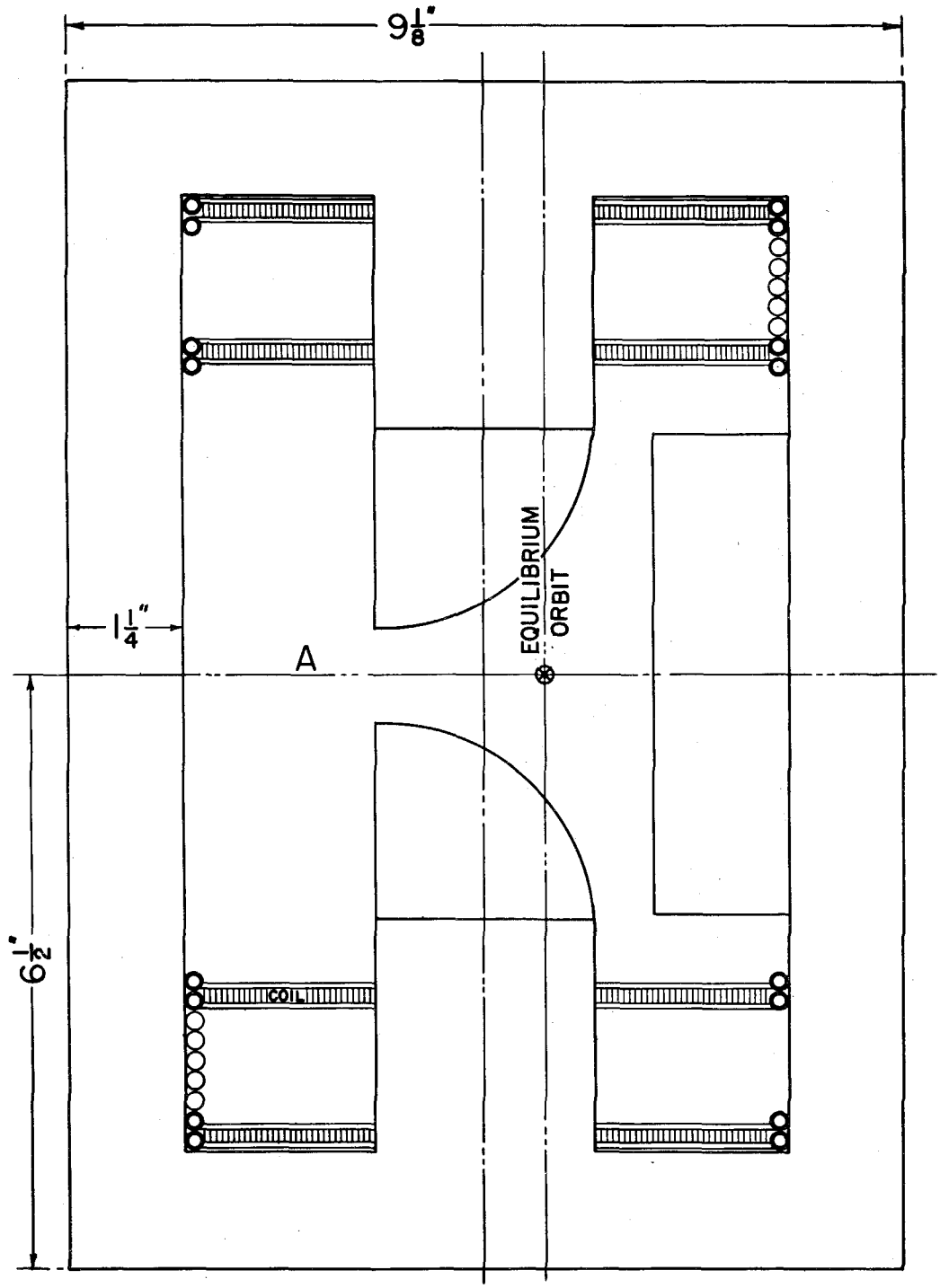

CROSS SECTION OF ENTRY MAGNET
Fig.8

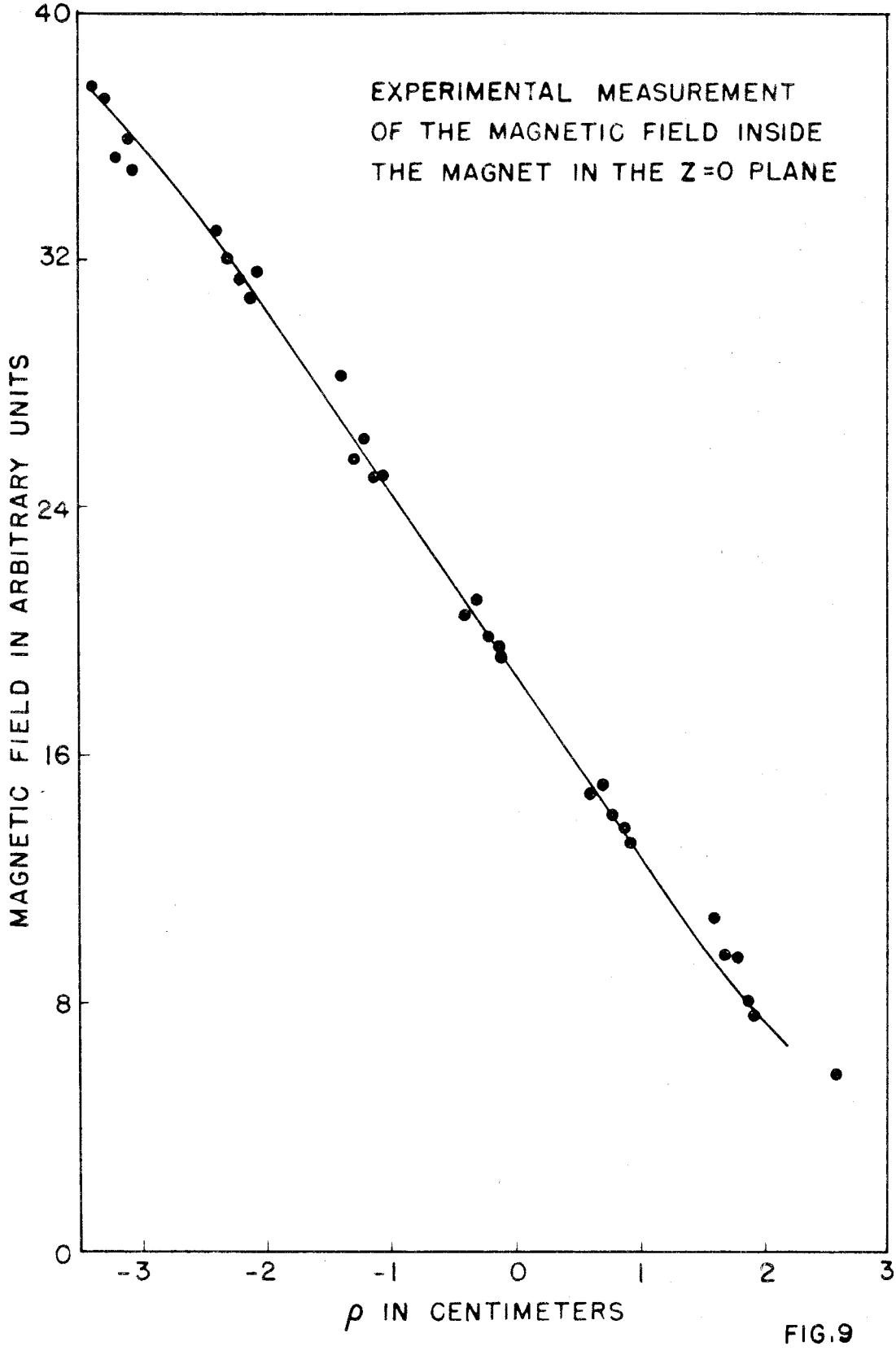
EXPERIMENTAL MEASUREMENT
OF THE MAGNETIC FIELD INSIDE
THE MAGNET IN THE Z=0 PLANE
MAGNETIC FIELD IN ARBITRARY UNITS
40
32
24
16
8
0
-3
-2
-1
0
1
2
3
ρ IN CENTIMETERS

FIG.9

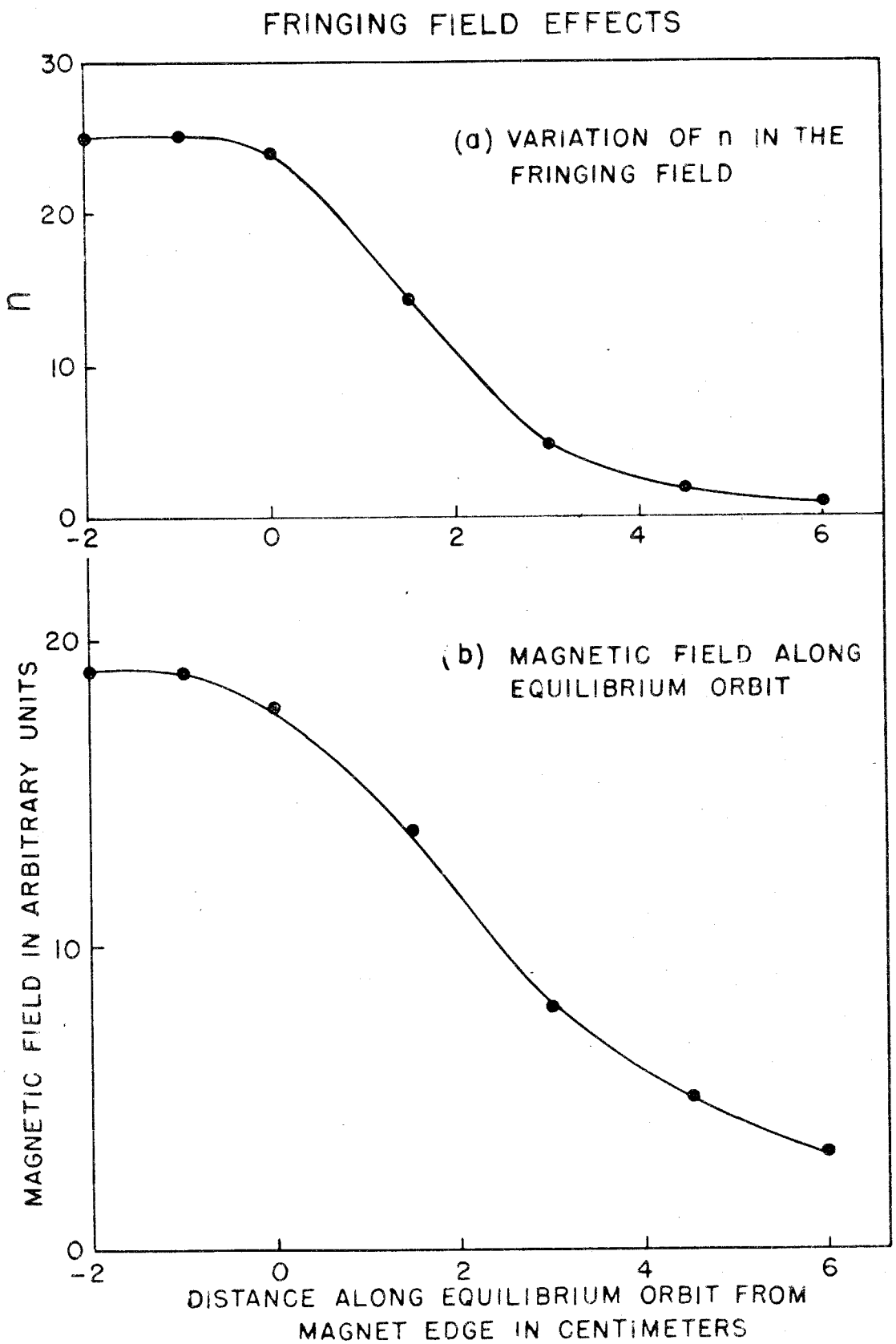
FRINGING FIELD EFFECTS
(a) VARIATION OF n IN THE FRINGING FIELD
n
30
20
10
0
-2
0
2
4
6
(b) MAGNETIC FIELD ALONG EQUILIBRIUM ORBIT
MAGNETIC FIELD IN ARBITRARY UNITS
20
10
0
-2
0
2
4
6
DISTANCE ALONG EQUILIBRIUM ORBIT FROM MAGNET EDGE IN CENTIMETERS

FIG.10

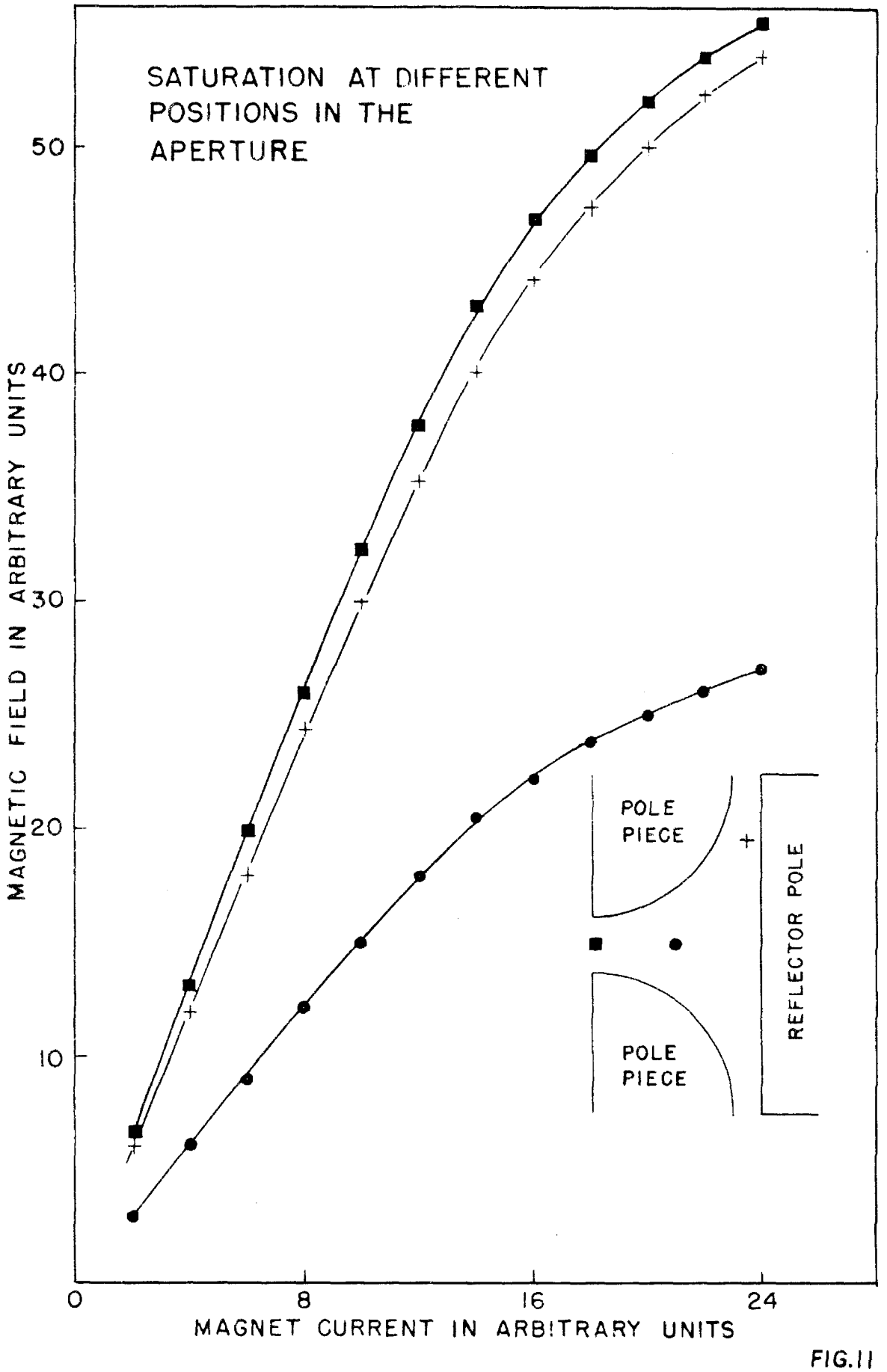
SATURATION AT DIFFERENT POSITIONS IN THE APERTURE
MAGNETIC FIELD IN ARBITRARY UNITS
10
20
30
40
50
0
8
16
24
MAGNET CURRENT IN ARBITRARY UNITS
POLE PIECE
POLE PIECE
REFLECTOR POLE

FIG.11

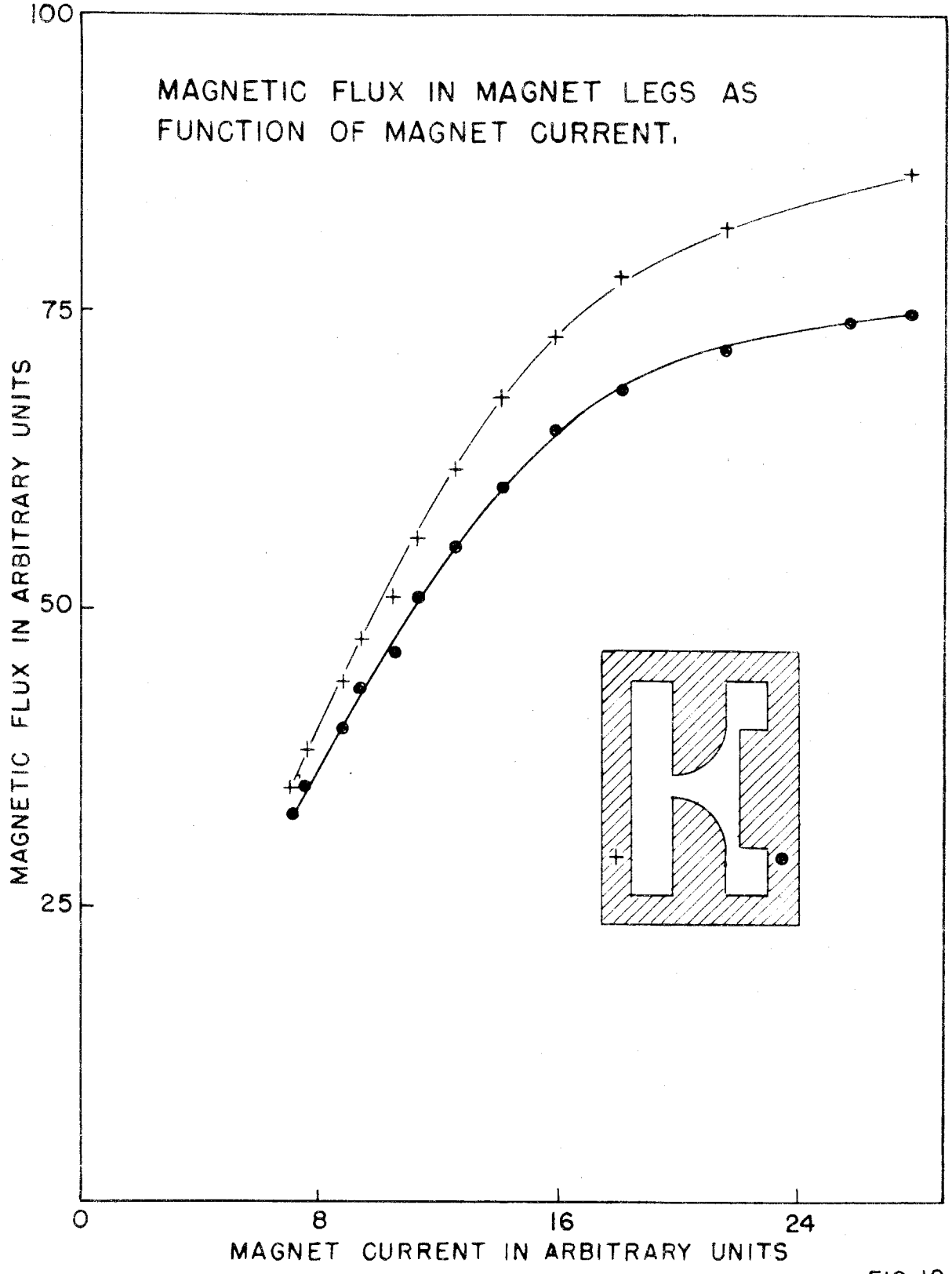
MAGNETIC FLUX IN MAGNET LEGS AS
FUNCTION OF MAGNET CURRENT.
100
75
50
25
0
8
16
24
MAGNETIC FLUX IN ARBITRARY UNITS
MAGNET CURRENT IN ARBITRARY UNITS

FIG. 12

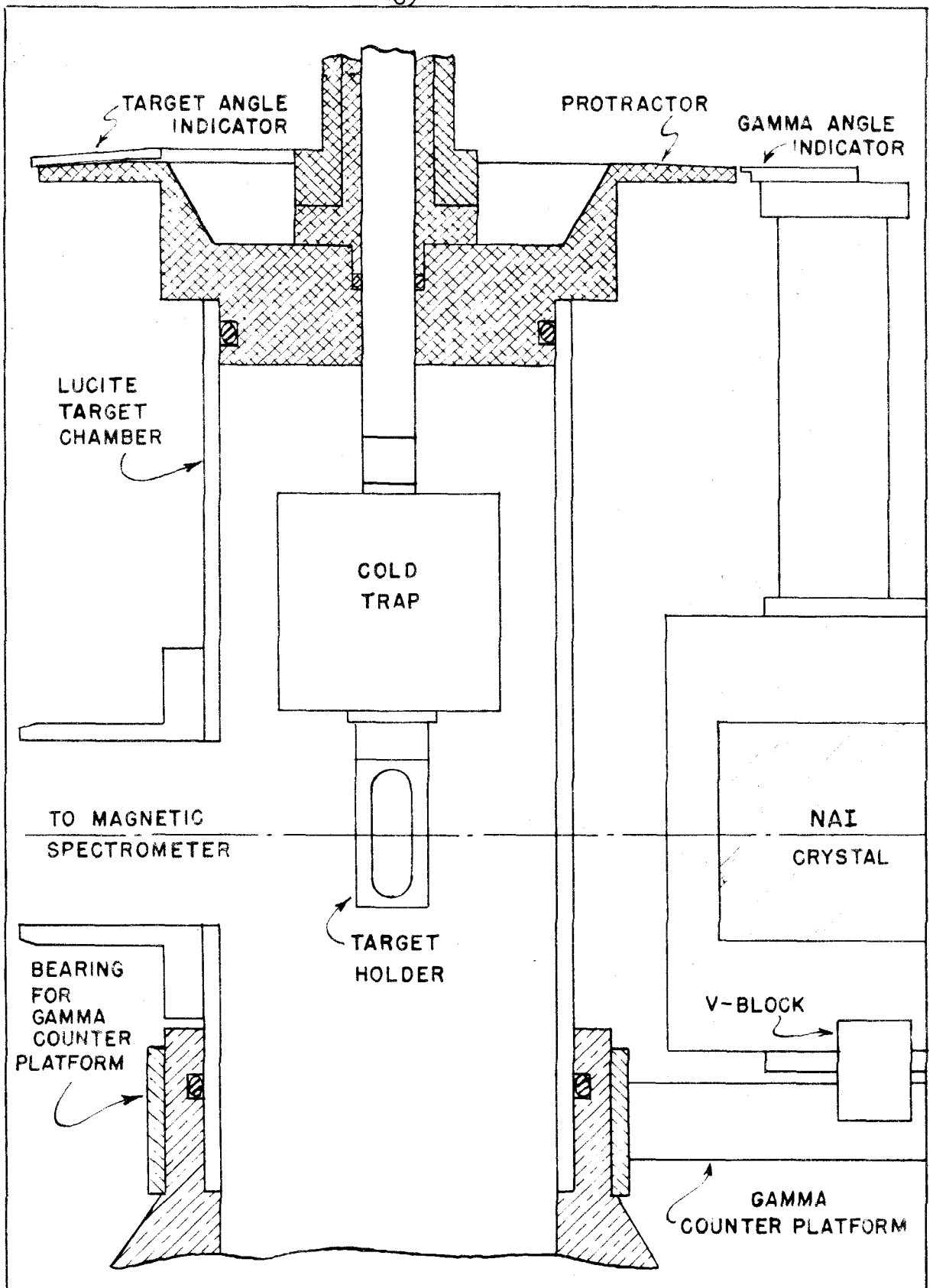

FRONT VIEW OF TARGET CHAMBER FIG. 13

FIG. 14– TOP VIEW OF TARGET CHAMBER

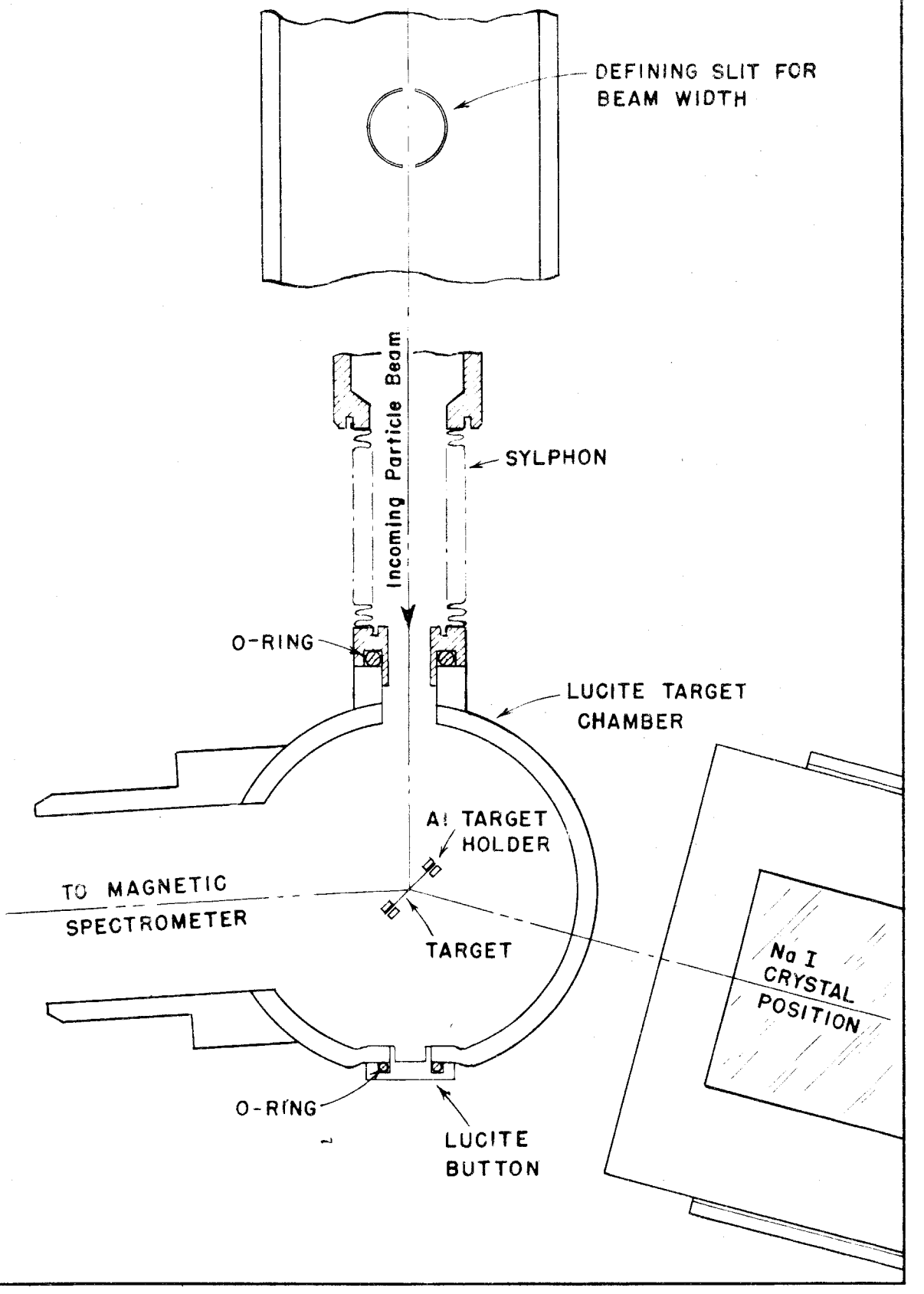

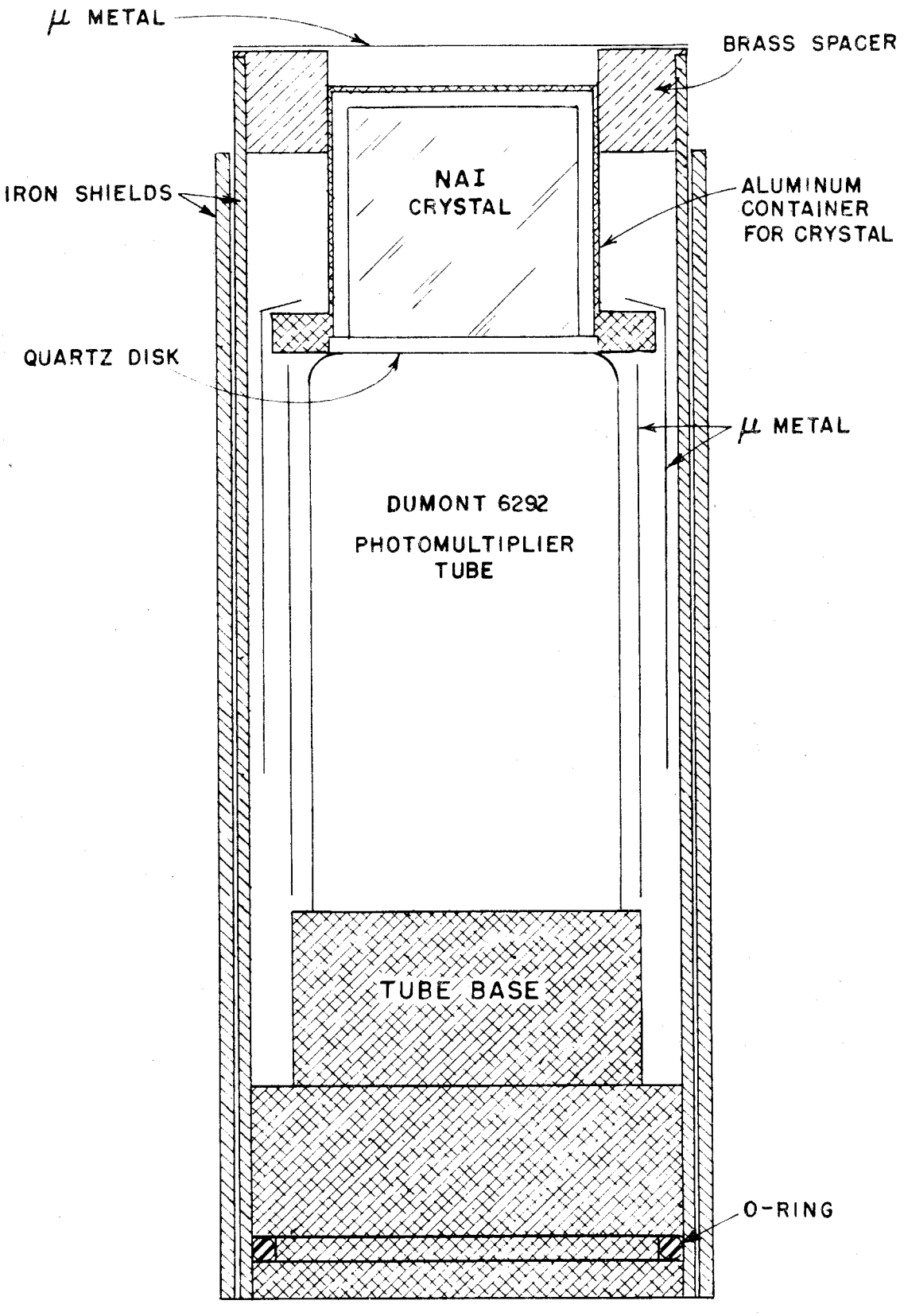
μ METAL
BRASS SPACER
IRON SHIELDS
NAI
CRYSTAL
ALUMINUM
CONTAINER
FOR CRYSTAL
QUARTZ DISK
μ METAL
DUMONT 6292
PHOTOMULTIPLIER
TUBE
TUBE BASE
O-RING

FIG. 15

(a) HORIZONTAL SLIT MEASUREMENTS

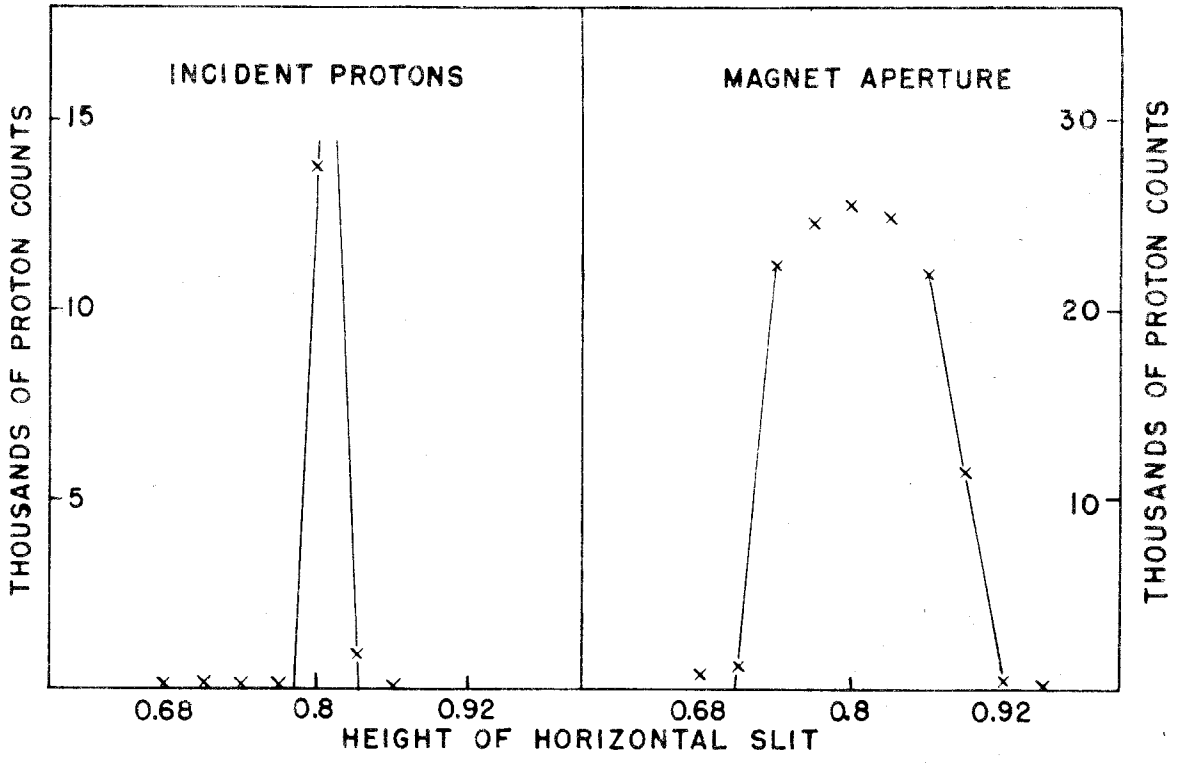

(b) VERTICAL SLIT MEASUREMENTS

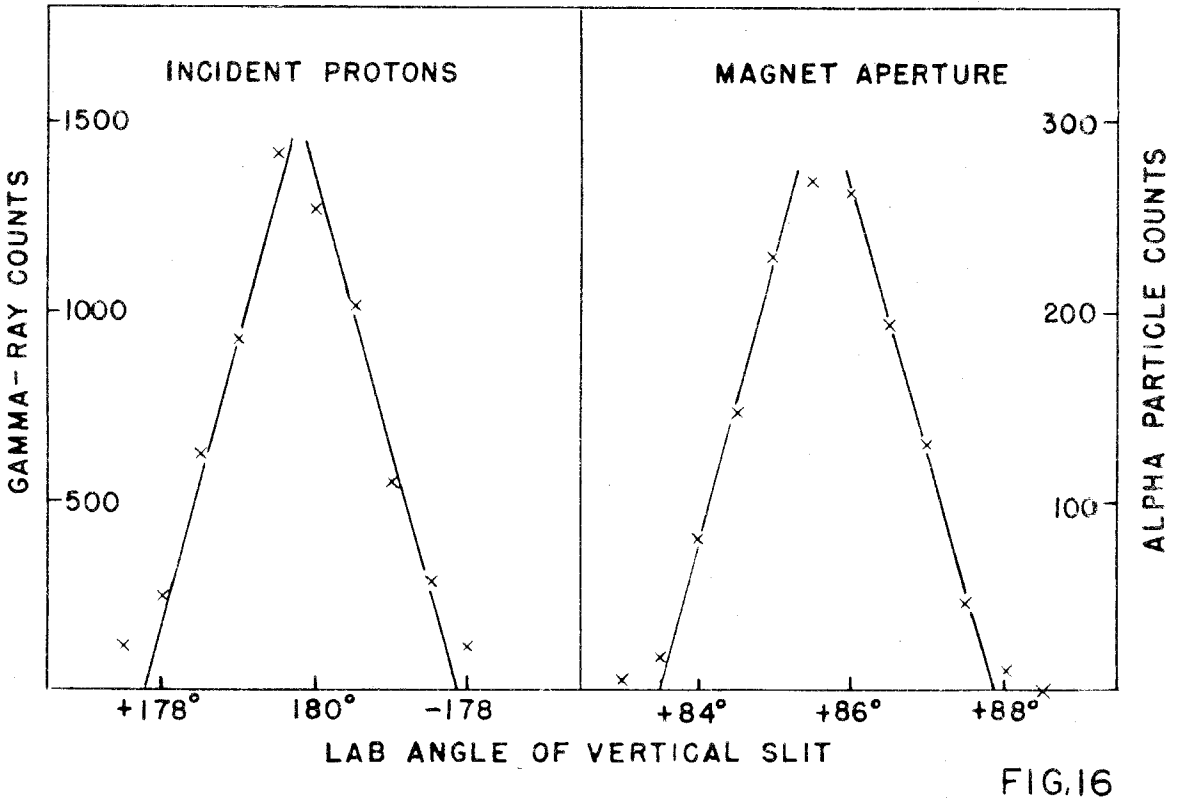

FIG. 16

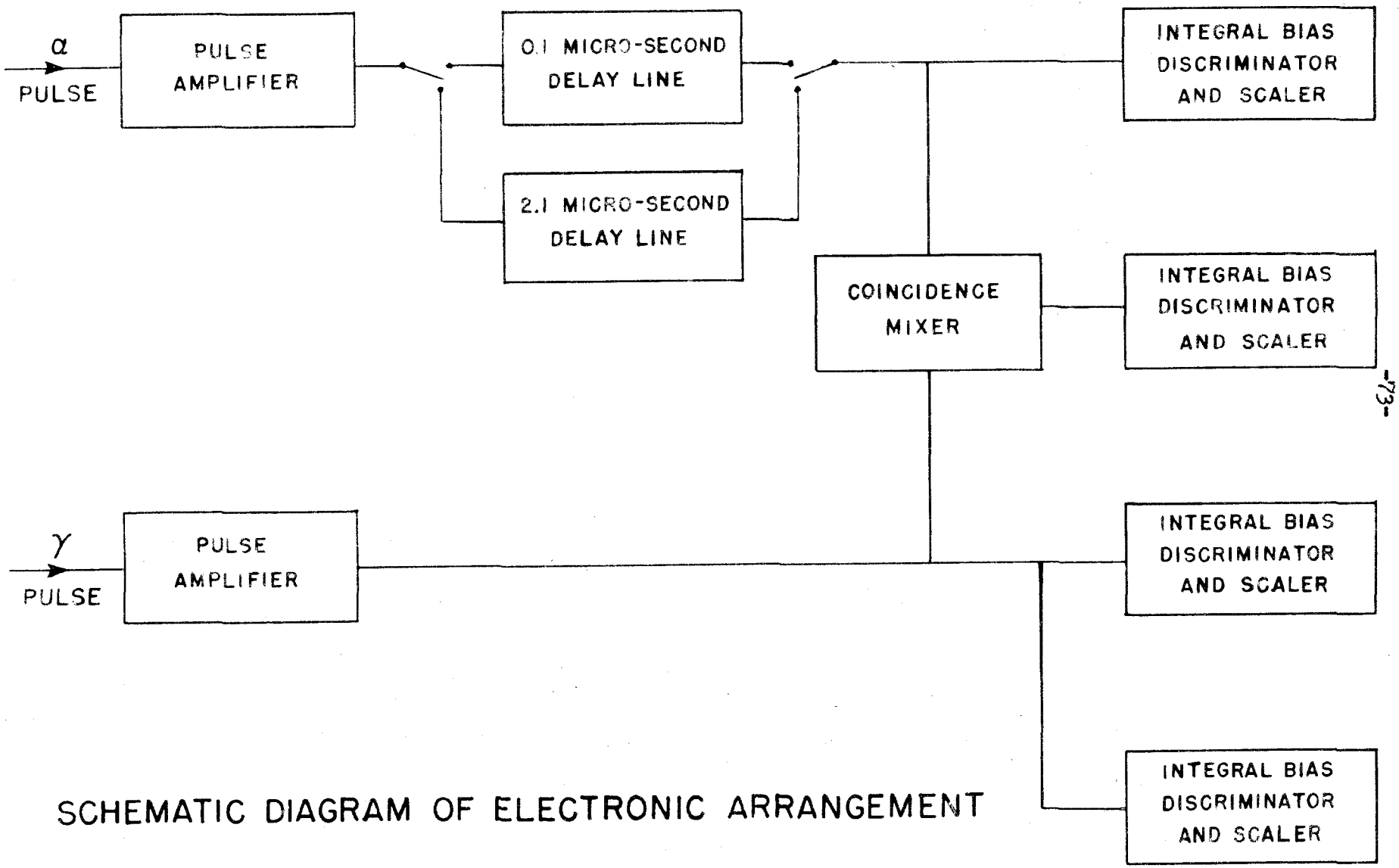

SCHEMATIC DIAGRAM OF ELECTRONIC ARRANGEMENT

FIG. 17

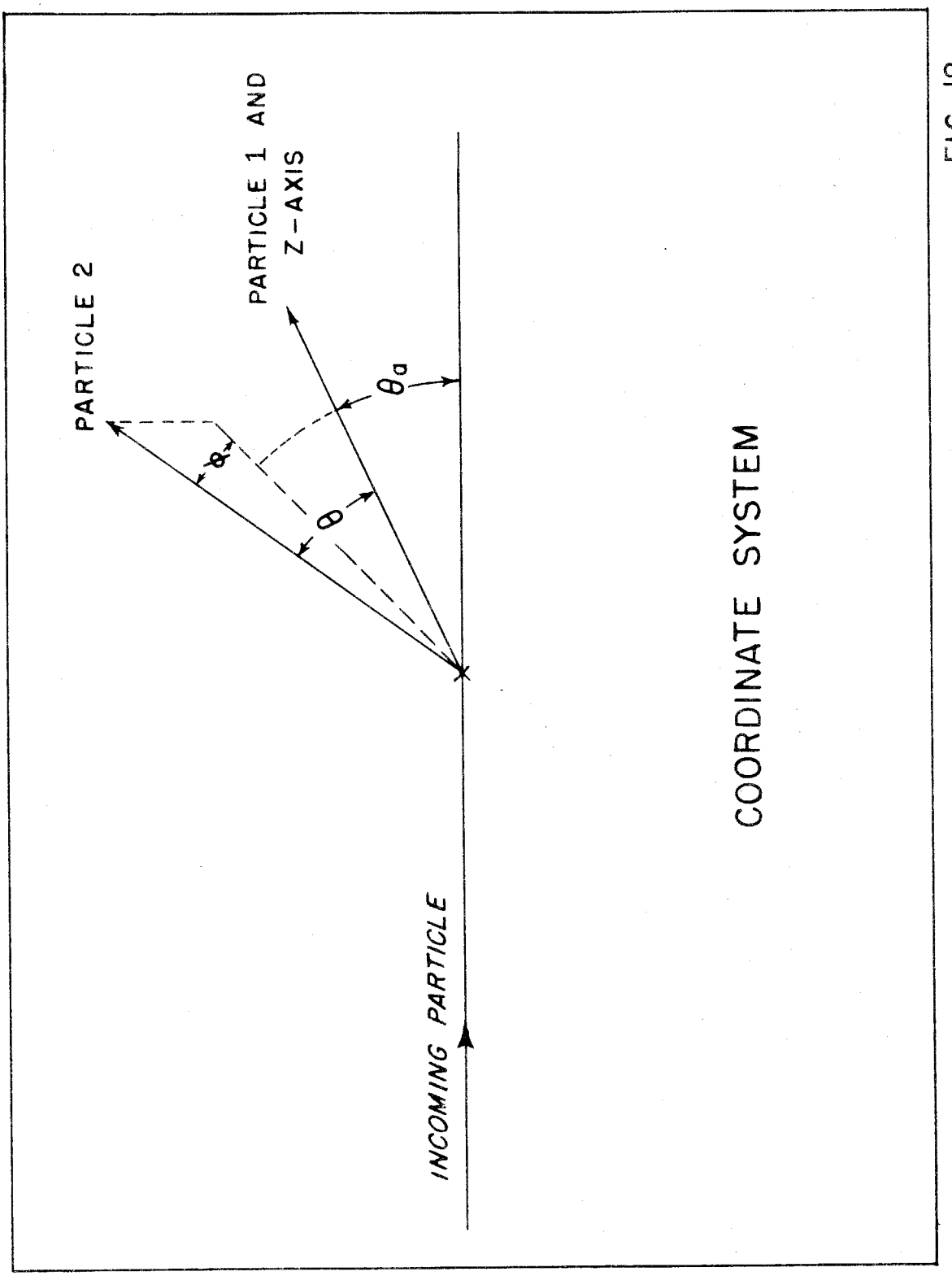
PARTICLE 2
PARTICLE 1 AND
Z-AXIS
θ_a
α
θ
INCOMING PARTICLE
COORDINATE SYSTEM

FIG. 18

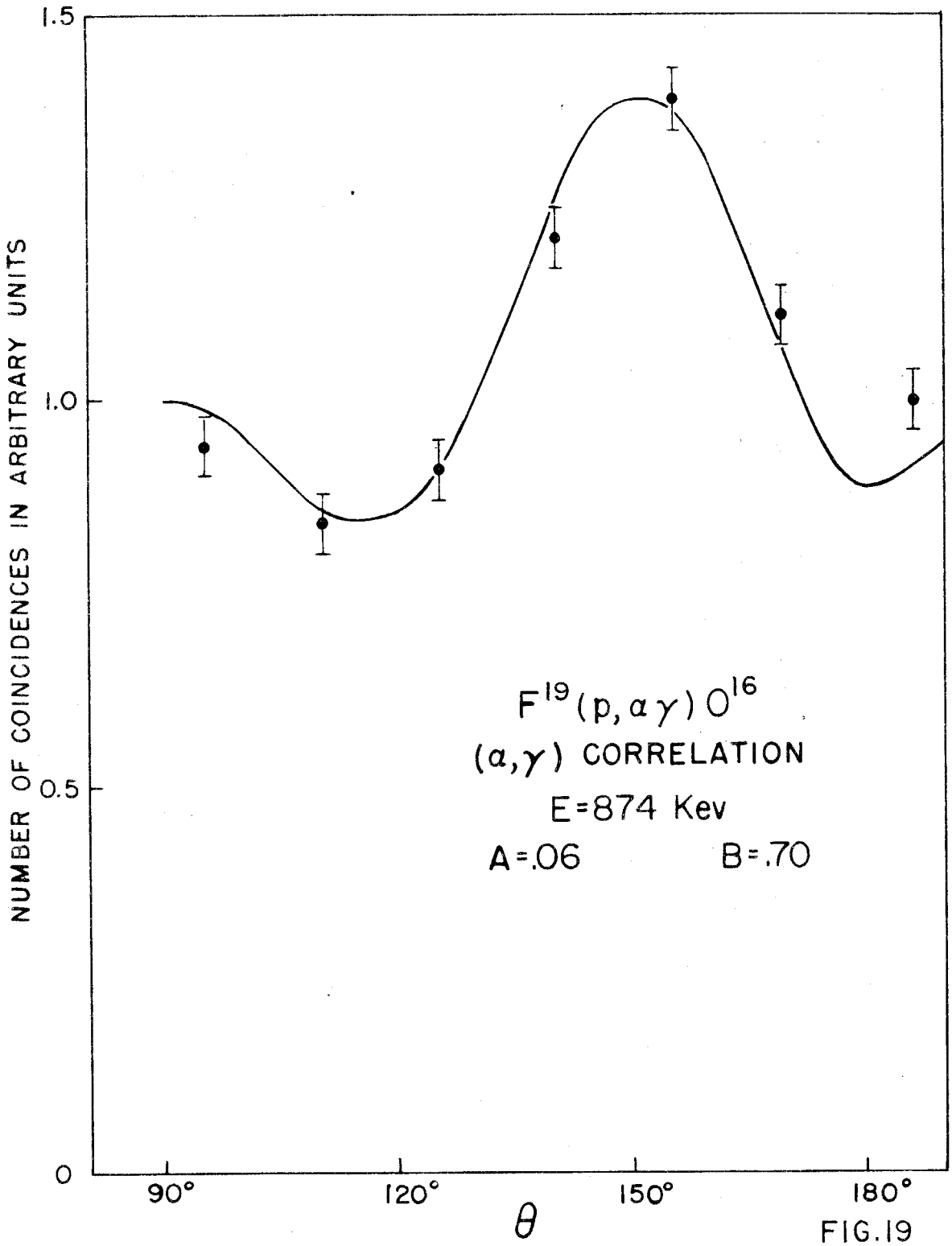
1.5
1.0
0.5
0
NUMBER OF COINCIDENCES IN ARBITRARY UNITS
90°
120°
150°
180°
θ
F19 (p, αγ) O16
(α,γ) CORRELATION
E=874 Kev
A=.06
B=.70

FIG.19

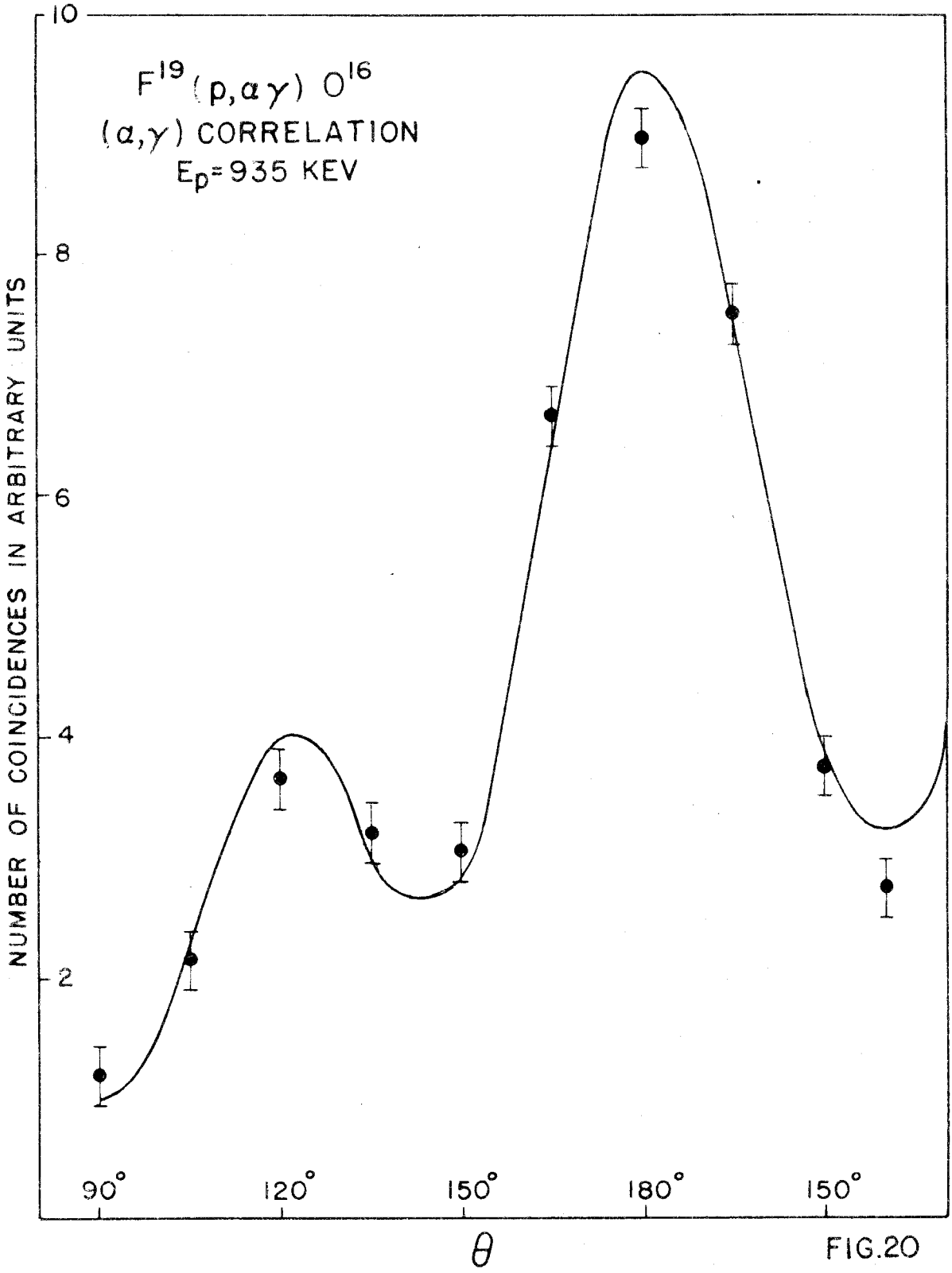
$F^{19}(p,\alpha\gamma)\,O^{16}$
(α,γ) CORRELATION
E_p=935 KEV
NUMBER OF COINCIDENCES IN ARBITRARY UNITS
10
8
6
4
2
90°
120°
150°
180°
150°
θ

FIG.20

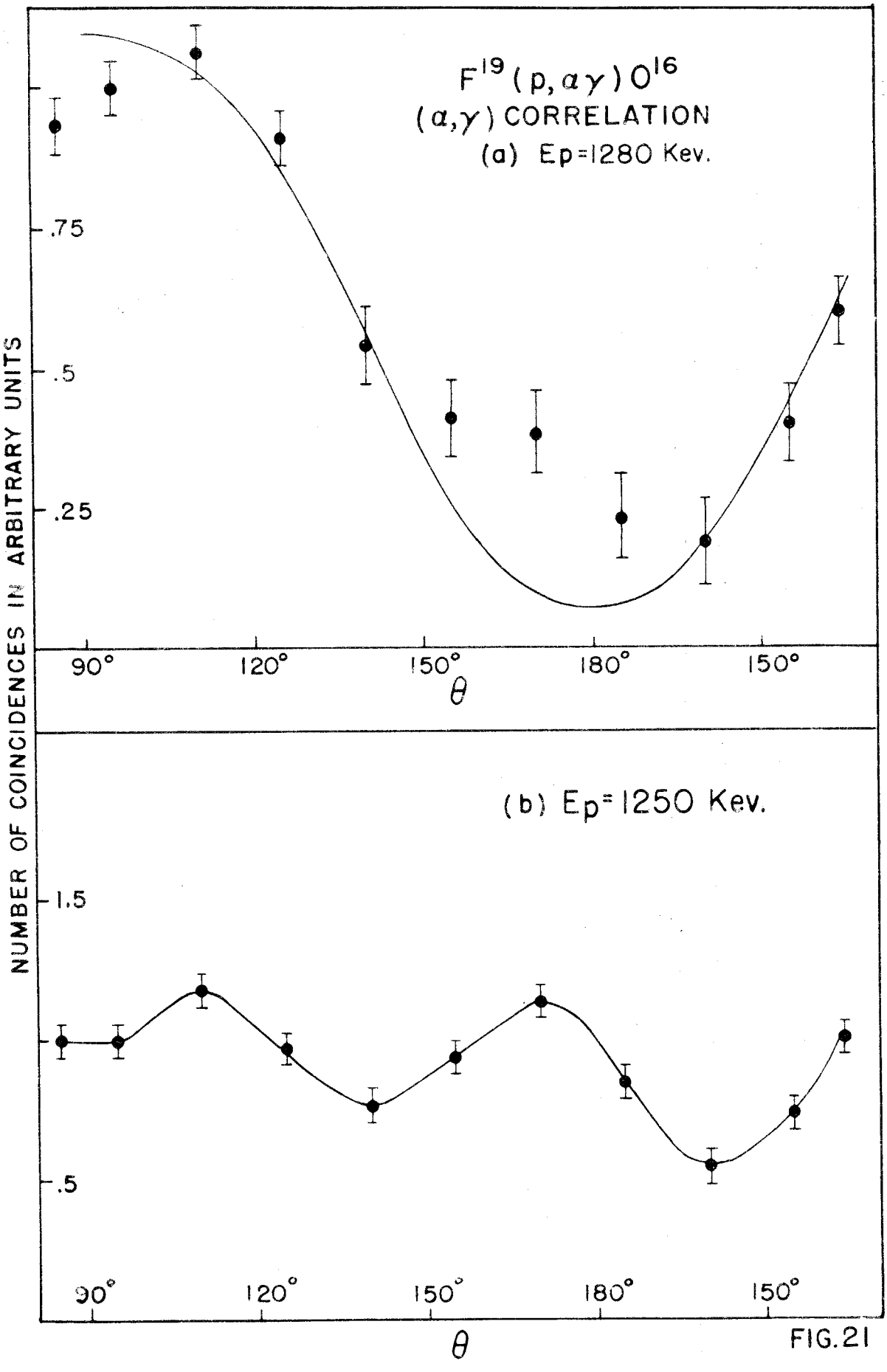
$F^{19}(p,\alpha\gamma)O^{16}$
(α,γ) CORRELATION
(a) Ep=1280 Kev.
.75
.5
.25
90°
120°
150°
180°
150°
θ
(b) Ep=1250 Kev.
1.5
.5
90°
120°
150°
180°
150°
θ
NUMBER OF COINCIDENCES IN ARBITRARY UNITS

FIG. 21

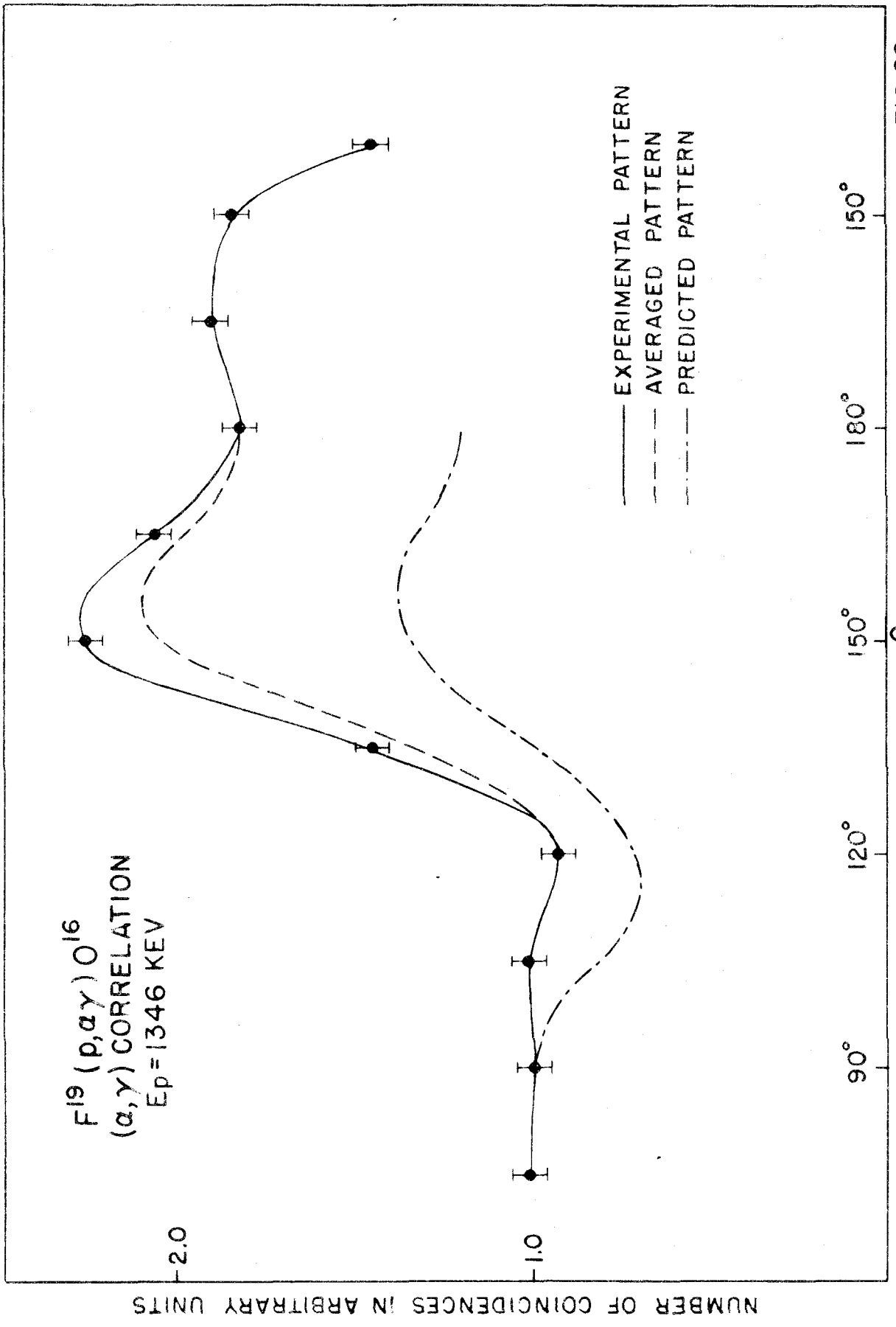
NUMBER OF COINCIDENCES IN ARBITRARY UNITS
2.0
1.0
90°
120°
150°
θ
150°
180°
EXPERIMENTAL PATTERN
AVERAGED PATTERN
PREDICTED PATTERN
F19 (p,αγ) O16
(α,γ) CORRELATION
Ep = 1346 KEV

FIG.22

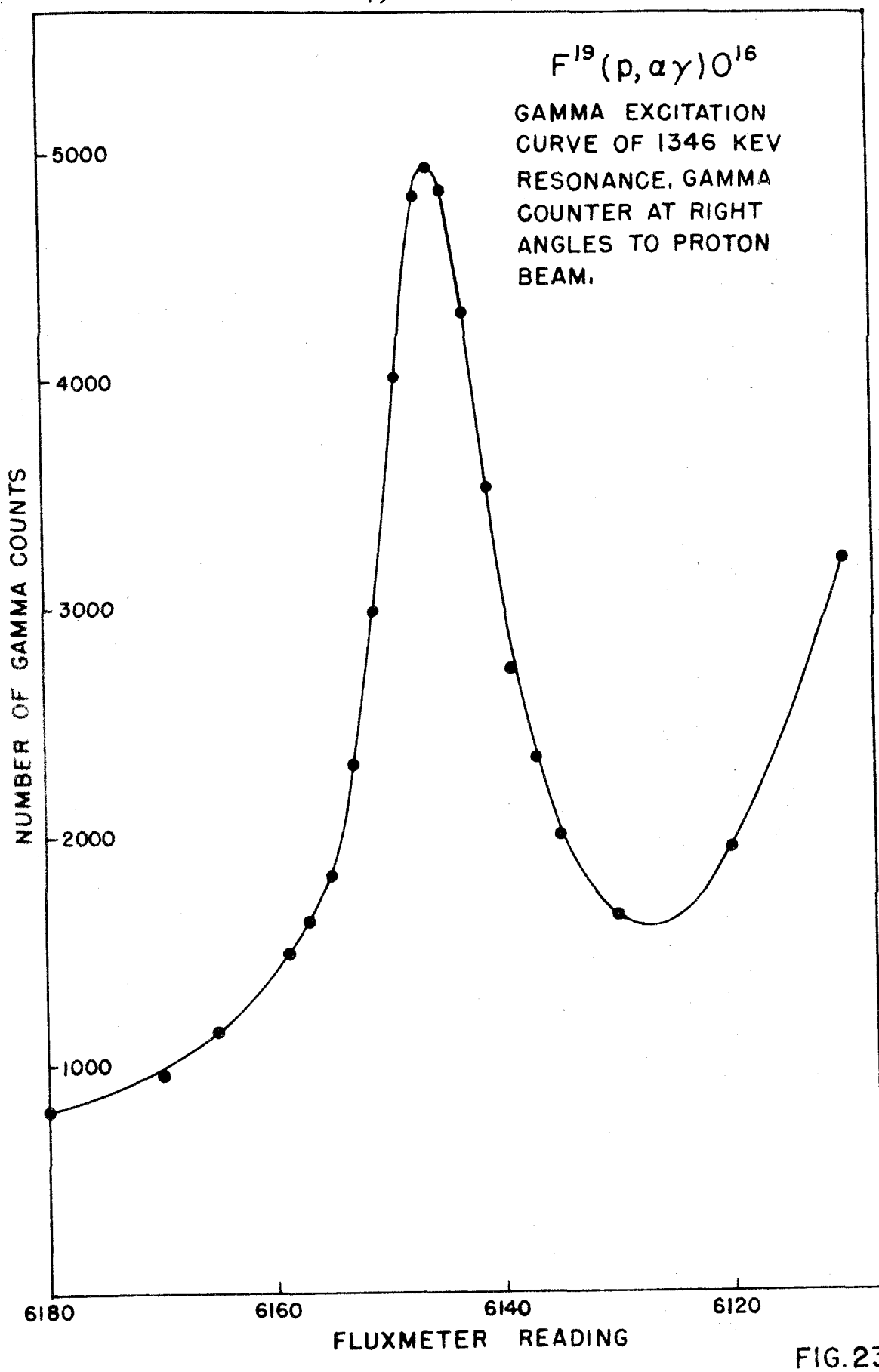
$F^{19}(p,\alpha\gamma)O^{16}$
GAMMA EXCITATION CURVE OF 1346 KEV RESONANCE. GAMMA COUNTER AT RIGHT ANGLES TO PROTON BEAM.
NUMBER OF GAMMA COUNTS
5000
4000
3000
2000
1000
6180
6160
6140
6120
FLUXMETER READING

FIG. 23

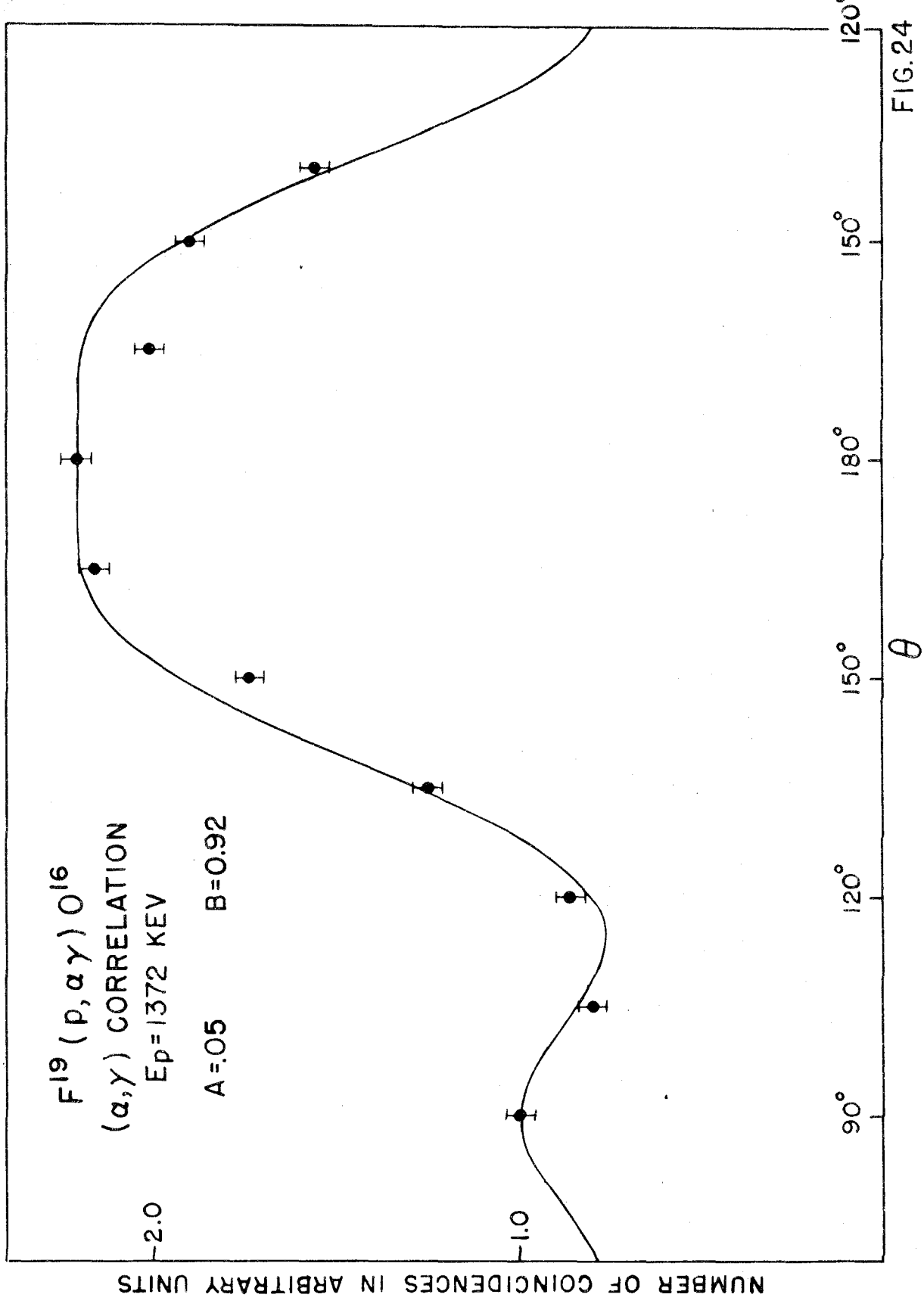
NUMBER OF COINCIDENCES IN ARBITRARY UNITS
2.0
1.0
90°
120°
150°
180°
150°
120°
θ
$F^{19}(p,\alpha\gamma)O^{16}$
(α,γ) CORRELATION
E_p=1372 KEV
A=.05
B=0.92

FIG.24